

1 **TITLE**

2 Climate-driven unsteady denudation and sediment flux in a high-relief unglaciated catchment-fan
3 using ^{26}Al and ^{10}Be : Panamint Valley, California

4
5 **AUTHORS**

6 Cody C. Mason* and Brian W. Romans

7 Department of Geosciences, Virginia Tech, Blacksburg, Virginia, 24061

8 *Corresponding Author: Cody C. Mason

9 Email: cmason80@vt.edu

10

11 **KEYWORDS**

12 Sediment Routing System, Catchment-fan, Signal Propagation, Paleodenudation, Climate,
13 Cosmogenic Radionuclides

14

15 **HIGHLIGHTS**

- 16 • $^{26}\text{Al}/^{10}\text{Be}$ Burial ages/paleodenudation rates measured in early to middle Pleistocene
17 alluvium
- 18 • Pleistocene paleodenudation averaged ~30 – 50% higher than modern ^{10}Be denudation
19 rates
- 20 • Maximum variability of +50/-33% from mean paleodenudation rate in unglaciated
21 catchment-fan
- 22 • 100 kyr Milankovitch periods may drive observable variability in CRN concentrations
- 23 • Limitations of $^{26}\text{Al}/^{10}\text{Be}$ method applied to alluvial fan stratigraphy are discussed

24

25 **ABSTRACT**

26 Environmental changes within erosional catchments of sediment routing systems are predicted to
27 modulate sediment transfer dynamics. However, empirical and numerical models that predict such
28 phenomena are difficult to test in natural systems over multi-millennial timescales. Tectonic
29 boundary conditions and climate history in the Panamint Range, California, are relatively well-
30 constrained by existing low-temperature thermochronology and regional multi-proxy paleoclimate
31 studies, respectively. Catchment-fan systems present there minimize sediment storage and
32 recycling, offering an excellent natural laboratory to test models of climate-sedimentary dynamics.
33 We used stratigraphic characterization and cosmogenic radionuclides (CRNs; ^{26}Al & ^{10}Be) in the
34 Pleasant Canyon complex (PCC), a linked catchment-fan system, to examine the effects of
35 Pleistocene high-magnitude, high-frequency climate change on CRN-derived denudation rates and
36 sediment flux in a high-relief, unglaciated catchment-fan system. Calculated $^{26}\text{Al}/^{10}\text{Be}$ burial ages
37 from 13 samples collected in an ~180 m thick outcropping stratigraphic succession range from ca.
38 1.55 ± 0.22 Ma in basal strata, to ca. $0.36 \pm 0.18 - 0.52 \pm 0.20$ Ma within stratigraphically highest
39 portions of the fan. The mean long-term CRN-derived paleodenudation rate, 36 ± 8 mm/kyr (1σ),
40 is higher than the modern rate of 24 ± 0.6 mm/kyr from Pleasant Canyon, and paleodenudation
41 rates during the middle Pleistocene display some high-frequency variability in the high end (up to
42 54 ± 10 mm/kyr). The highest CRN-derived denudation rates are associated with stratigraphic
43 evidence for increased precipitation during glacial-pluvial events after the middle Pleistocene
44 transition (post ca. 0.75 Ma), suggesting 100 kyr Milankovitch periodicity could drive the observed
45 variability. We investigated the potential for non-equilibrium sedimentary processes, *i.e.* increased
46 landslides or sediment storage/recycling, to influence apparent paleodenudation rates; end-
47 member mixing models suggest that a mixture of >50% low-CRN-concentration sediment from

48 landslides is required to produce the largest observed increase in paleodenudation rate. The overall
49 pattern of CRN-derived burial ages, paleodenudation rates, and stratigraphic facies suggests
50 Milankovitch timescale climate transitions drive variability in catchment denudation rates and
51 sediment flux, or alternatively that climate transitions affect sedimentary process regimes that
52 result in measurable variability of CRN concentrations in unglaciated catchment-fan systems.

53

54 **1.0 INTRODUCTION**

55 Sediment routing systems consist of an erosional zone, a fluvial transfer zone, and a
56 depositional basin (Allen, 2008). The creation and preservation of stratigraphy within a sediment
57 routing system is the sum of complex processes including up-system environmental changes in the
58 erosion zone, sediment storage and recycling in the erosion and/or fluvial transfer zones, and
59 changes in accommodation and intrinsic system dynamics in depositional basins (Paola et al.,
60 1992). Some geoscientists have conceptualized sediment production, transport, storage, and
61 remobilization dynamics along sediment routing systems in terms of environmental signal
62 propagation (Castelltort and Van Den Driessche, 2003; Romans et al., 2016). In this framework,
63 sediment flux is the carrier of environmental change signals. Inverting sediment flux from
64 stratigraphy is thus complicated by issues including signal to noise ratio, signal delay, signal
65 attenuation, or signal ‘shredding’, and combinations of these phenomena may preclude
66 preservation or inversion of up-system environmental change from depositional products
67 (Jerolmack and Paola, 2010; Romans et al., 2016). Given this context, *a priori* assumptions of
68 minimal signal delay, attenuation, or shredding are required to explore effects of up-system drivers
69 on magnitude and variability of signals of erosion-deposition dynamics. A steep catchment-fan
70 system with a continuously subsiding depositional segment represents an ideal natural laboratory

71 for the investigation of sedimentary signal propagation because: (1) it may react rapidly to changes
72 in boundary conditions, (2) it likely experiences minimal signal delay or attenuation because it
73 lacks, or has a very short transfer zone, and (3) rapidly subsiding alluvial basins contain relatively
74 complete records of past surface dynamics (Straub and Esposito, 2013). Catchment-fan systems
75 have previously been used to explore effects of environmental change on catchment erosion,
76 sediment flux, and sediment caliber exiting catchments (Fig. 1) (Allen and Densmore, 2000;
77 Densmore et al., 2007; Armitage et al., 2011). In such a framework, changes in erosion and
78 sediment flux from catchment to fan are direct signals of environmental change in a catchment. A
79 fundamental question then is what are the magnitudes of signals emitted from the erosive source
80 of a natural catchment-fan system? And a related question is by how much do such magnitudes
81 vary through time? Placing constraints on denudation rate variability — a proxy for sediment
82 supply at a catchment outlet — through time, in a single sediment routing system, allows for the
83 examination of signals of environmental change.

84 Predicting catchment response to environmental change, specifically climatic transitions,
85 on a global to individual catchment basis is challenging, because with several exceptions there is
86 a lack of empirical data sets that constrain high-resolution and long-term (10^{3-4} yr and 10^6 yr,
87 respectively) records of changes in catchment-scale erosion or sediment flux (Granger and
88 Schaller, 2014; Puchol et al., 2016; Oskin et al., 2017). Researchers have addressed this topic by
89 measuring CRNs in alluvial and lacustrine stratigraphy to derive a time series of paleodenudation
90 rates (Balco and Stone, 2005; Granger and Schaller, 2014), by utilizing volumetric estimates of
91 basin fill (Covault et al., 2011), or by analyzing provenance of dated sedimentary deposits
92 spanning climatic transitions (Mason et al., 2017). Results indicate many glaciated sediment
93 routing systems have responded to changing climatic boundary conditions within resolution of the

94 various chronometers (Stock et al., 2005; Glotzbach et al., 2013; Marshall et al., 2015; Gulick et
95 al., 2015; Mason et al., 2017), whereas other records from glaciated and unglaciated systems show
96 a complex response, or a lack of any measurable change in denudation rate or fluxes to basins
97 across major climate transitions (Granger et al., 2001; Oskin et al., 2017). For instance, in the
98 Tibetan Plateau, ^{10}Be -derived denudation rates across the Plio-Pleistocene transition show a
99 complex, asynchronous, or weak transient response to onset of glaciation (Puchol et al., 2016). In
100 the unglaciated Peninsular Ranges of southern California, ^{10}Be -derived paleodenudation rates
101 across the Plio-Pleistocene transition (ca. 4 – 1 Ma) remained constant (Oskin et al., 2017).
102 However, in the unglaciated Northern Kenya Rift erosion/deposition rates saw a significant
103 transient increase during the African Humid Period, between ca. 5 – 15 ka, (Garcin et al., 2017),
104 and tectonically quiescent, unglaciated sediment routing systems along the Texas Gulf Coast
105 responded to interglacial warm periods with increased CRN-derived denudation rates (Hidy et. al.,
106 2014). Yet in the Pacific Northwest, periglacial conditions during the last glacial maximum
107 increased CRN-derived denudation rates relative to the Holocene (Marshall et al., 2015). These
108 results highlight the complexity in natural system response to changing climate, complicate
109 interpretations of sedimentary records of environmental change, and prediction of system response
110 to future global climate change.

111 Numerical simulations of linked catchment-fan systems represent a tool to bridge the gap
112 between modern and geologic-timescale empirical studies, and may be used to explore effects of
113 up-system forcings on depositional products. Simulations typically impose changes in catchment
114 or orogen-scale boundary conditions — often precipitation and fault-slip rate (Fig. 1) — and
115 measure various model outputs including channel incision rate, catchment denudation, sediment
116 flux at catchment outlets, and spatial distribution of grain-size variations in the depositional

117 segment (Allen and Densmore, 2000; Armitage et al., 2011). Such studies predict distinct
118 timescales of system response and equilibrium for various forcings, with reaction timescales to
119 perturbations in precipitation occurring over $\sim 10^{3-4}$ yrs, and reaction timescales to tectonic
120 perturbations occurring over 10^{5-6} yrs (Fig. 1) (Allen, 2008; Armitage et al., 2011). Crucially,
121 models that modulate precipitation rates mimicking Milankovitch-timescale climate change result
122 in concomitant modulation of catchment denudation rates and sediment fluxes (Allen and
123 Densmore, 2000), and CRN concentrations may respond to changes in erosion rates over multi-
124 millennial timescales (Fig. 1c). To test the predictions of numerical models in natural systems, two
125 fundamental conditions must be met: (1) tectonic and paleoclimatic boundary conditions should
126 be relatively well constrained, and (2) the system must preserve a stratigraphic record of changes
127 in denudation rates, sediment flux, or depositional volumes through time.

128 In this paper, we place new constraints on CRN-derived signals of denudation rate
129 variability over multi-millennial timescales in a steep, unglaciated, catchment-fan system within
130 an uplifted normal fault block in Panamint Valley, California. This configuration is common to
131 much of the American Great Basin, Basin and Range of the United States and Mexico, and
132 elsewhere globally, yet is underrepresented in existing literature. We present new data and
133 interpretations from 13 CRN samples collected throughout a 180-m thick succession of
134 outcropping Pleistocene alluvial-lacustrine strata, and from two samples of modern sediment
135 collected at feeder catchment outlets. This empirical record of CRN-derived denudation rate and
136 sediment supply, as stored in the depositional segment of a linked catchment-fan, represents a test
137 of conceptual, numerical, and empirically derived predictions for the effects of multi-millennial
138 timescale climate change on catchment-erosion and fan-deposition dynamics.

139

140 **2.0 BACKGROUND**

141 **2.1 Pleasant Canyon Complex Source-to-Sink Parameters**

142 The Panamint Range and Valley are located in eastern California, west of Death Valley
143 and east of the Argus and Slate Ranges (Fig. 2). The Pleasant Canyon complex (PCC) lies at the
144 terminus of a high-relief catchment (~2350 meters) that drains 32.8 km² of the central Panamint
145 Range. Figure 3 displays catchment parameters including elevation, surface slope, geology and
146 hypsometry for Pleasant Canyon. The bedrock lithologies of Pleasant Canyon are primarily quartz-
147 bearing Proterozoic-aged metamorphic, igneous, and sedimentary units, with the exception of
148 restricted exposures of the Sentinel Peak member of the Noonday Dolomite (Fig. 3c) (Albee et al.,
149 1981). The contact between World Beater Gneiss and Proterozoic sedimentary units in the upper
150 reaches of Pleasant Canyon (Figure 3c) corresponds to a decrease in slope associated with minor
151 Pleistocene to Holocene alluvial deposits (Albee et al., 1981).

152 The exhumed depositional segment of the PCC is positioned at the mouth of Pleasant
153 Canyon (Figs. 2 and 3) and is composed of ~180 m of mixed alluvial and lacustrine deposits of
154 Pleistocene age (Smith, 1976; Vogel et al., 2002). Stratigraphic surfaces in the PCC were once
155 active alluvial fan, subaqueous lake bed, or playa floor environments. Deposits aggraded during
156 progressive burial via tectonic subsidence, followed by Pleistocene exhumation and inversion
157 along a series of high-angle normal faults known as the Panamint Valley fault zone (Fig. 2)
158 (Cichanski, 2000; Vogel et al. 2002). The timing of localized high-angle faulting and inversion of
159 PCC deposits is constrained only by the unknown age of the youngest abandoned alluvial fan
160 surfaces. Small headward eroding gullies have formed since exhumation, and now afford excellent
161 3-D exposures of PCC stratigraphy.

162

163 2.2 Late Cenozoic Tectonic History

164 The tectonic history of the Panamint Mountains is a first-order control on the pace of
165 catchment denudation and sediment flux to linked alluvial fans (Allen and Densmore, 2000). The
166 Panamint Mountains (Fig. 2) are located within the eastern California-Walker Lane shear zone, a
167 region of diffuse dextral plate boundary deformation east of the San Andreas Fault. Panamint
168 Valley is defined by active structures displaying complex Plio-Quaternary deformation patterns;
169 eastern Panamint Valley is bound by the low-angle Panamint-Emigrant detachment system
170 exposed along, or at low elevation within, the Panamint rangefront (Fig. 2). Active deformation is
171 potentially mainly accommodated by a second set of high-angle oblique dextral faults, the
172 Panamint Valley fault zone, which has cut and displaced Pleistocene to Holocene alluvium
173 exposed along eastern Panamint Valley and the western Panamint rangefront (Fig. 2; Cichanski,
174 2000). The western Panamint Valley is structurally bound by the dextral-oblique Ash Hill fault
175 system near the eastern foot of the Argus Range (Fig. 2) (Densmore and Anderson, 1997).

176 Early tectonic exhumation and uplift of the Panamint Mountains may have initiated along
177 a single west-dipping, west-side-down, master detachment fault—the Panamint-Emigrant
178 detachment fault (Fig. 2)—starting close to ca. 12 Ma (Bidgoli et al., 2015). Low-temperature
179 thermochronometry (zircon U-Th/He) from the central Panamint Range shows exhumation-related
180 cooling initiated after ca. 12 Ma, while lower temperature thermochronometers (apatite U-Th/He)
181 cluster at ca. 4 Ma, and support rapid Pliocene cooling and tectonic exhumation of the Panamint
182 Range, potentially associated with the initiation of the dextral oblique Panamint Valley fault zone
183 (Bidgoli et al., 2015). Sediment accumulation within the Nova Basin in northeast Panamint Valley
184 occurred between ca. 4.4 – 3 Ma, consistent with Pliocene tectonic rejuvenation (Fig. 2) (Snyder
185 and Hodges, 2000).

186 Pleistocene to recent rates of dip-slip motion for the Panamint Valley fault zone near
187 Ballarat are $\sim 0.35 - 1$ mm/yr (Fig. 2), and were derived using detrital zircon maximum depositional
188 ages from basal stratigraphy of the PCC (Vogel et al., 2002). Dextral deformation rates along the
189 Panamint Valley fault zone are debated, but are thought to be between 1 – 4 mm/yr (Smith, 1976;
190 Oswald and Wesnousky, 2002). Given available information, early to middle Pleistocene
191 catchment denudation rates should reflect equilibrium with respect to uplift patterns of the central
192 Panamint Range since ca. 3 – 4 Ma (Fig. 1) (Allen and Densmore, 2000; Densmore et al., 2007;
193 Armitage et al., 2011).

194

195 **2.3 Pleistocene Climate History**

196 Panamint Valley is an arid to semi-arid endorheic basin located in a major rain shadow east
197 of the Sierra Nevada Range. Precipitation is scarce at low elevations in Panamint Valley, but
198 increases with elevation in a semi-logarithmic manner in the Panamint Range (Jayko, 2005). The
199 Wildrose Ranger station (1250 m asl) in the northern Panamint Range receives an average of 19
200 cm of precipitation annually (Jayko, 2005). No long-term record of precipitation exists for Pleasant
201 Canyon, but the mean elevation of ~ 1700 m asl likely results in $>25 - 35$ cm of mean annual
202 precipitation. Observations of modern sedimentation events in Death and Panamint Valley indicate
203 catchment hillslopes and fluvial channels transmit material to alluvial fans during low-frequency,
204 high-magnitude storm events. Thus, long-term trends in major storm frequency may influence
205 sediment transfer from catchment to fan.

206 Pleistocene climate in the Great Basin was on average wetter and colder than the late
207 Holocene interglacial (See inset map from Fig. 2; Oster et al., 2015). Pluvial lakes filled Panamint
208 Valley multiple times during the Pleistocene (Smith, 1976) via increased local precipitation and

209 runoff from the paleo Owens River system (Jannik et al., 1991; Phillips, 2008). Continental
210 paleoclimate records including pollen, hydrological restorations of pluvial lakes, oxygen isotope
211 data, and mass-balance models of Pleistocene Sierra Nevada glaciers agree that temperatures
212 during the last glacial maximum were $\sim 5 - 6^{\circ}\text{C}$ colder, and precipitation was up to 2x greater than
213 during the late Holocene (D’Arcy et al., 2016, and references therein). Mid-glacial climate
214 conditions typify most of the Pleistocene, and were $2 - 3^{\circ}\text{C}$ colder with precipitation rates $\sim 1.5\text{x}$
215 those of modern conditions (D’Arcy et al., 2016). D’Arcy et al. (2016) found that Late Pleistocene
216 climatic forcing, specifically increased precipitation, resulted in measurable differences in patterns
217 of down-system fining of alluvial sediments on Death Valley fans, corresponding to an $\sim 20\%$
218 increase in Pleistocene catchment-fan sediment flux.

219

220 **2.4 Previous Regional Paleodenudation Studies**

221 The ages of alluvial fans in the Death Valley area have been used to understand rates of
222 tectonic deformation and effects of climate on alluvial fan morphology (Frankel et al., 2007).
223 Unfortunately, few employed catchment-wide paleodenudation rate techniques. Frankel et al.
224 (2007) dated faulted alluvial fans in northern Death Valley using ^{36}Cl depth profiles, and used
225 inherited concentrations to derive paleodenudation rates of ~ 40 and ~ 80 mm/kyr for two
226 catchment-fan systems along the western Grapevine Mountains during the last mid-glacial (ca. 70
227 ± 10 ka).

228 Alluvial fan volumetric estimates and rough age constraints were used to quantify time-
229 averaged denudation rates for catchments along the western Panamint Range; results suggest
230 denudation rates between $\sim 40 - 230$ mm/kyr. Jayko (2005) used these results to suggest higher
231 precipitation may lead to higher sediment flux in the western Panamint Range. We note that

232 differential slip rates along the range-bounding faults would play a fundamental role in controlling
233 relief and slope, both of which may correlate positively to higher denudation rates. A time series
234 of denudation rates from a single high-relief, unglaciated catchment within the Great Basin
235 represents a crucial missing component to understanding variability of erosion-deposition
236 dynamics across glacial-interglacial climate transitions.

237

238 **3.0 METHODS**

239 **3.1 Sedimentary Lithofacies & Stratigraphic Architecture**

240 We characterized the stratigraphy of the PCC using measured lithostratigraphic sections,
241 and high-resolution photopanoramas for inaccessible outcrops. For our two measured sections
242 (Fig. 2b), stratigraphy and sedimentology were characterized at the cm to decimeter scale. We
243 recorded dominant grain size, bed thickness, sedimentary structures, sorting, particle roundness,
244 clast vs. matrix support, and lateral continuity of beds, and constructed lithofacies and lithofacies
245 associations that were used to interpret depositional environments (See Supplementary material
246 S2).

247

248 **3.2 Field Sampling, Laboratory Preparation, and Measurement of Cosmogenic $^{26}\text{Al}/^{10}\text{Be}$**

249 We took advantage of the linked nature of the Pleasant Canyon catchment-fan system by
250 collecting quartz-rich sediment in a vertical succession from Pleistocene alluvium derived directly
251 from Pleasant Canyon. Samples taken vertically through a stratigraphic succession represent a
252 record of catchment denudation rates through time (*e.g.* Balco and Stone, 2005). All samples were
253 located within, or stratigraphically correlated to our measured sections (locations depicted in Fig.
254 2b).

255 Our sampling strategy was designed to minimize effects of modern exposure to cosmic
256 rays (similar to that of Puchol et al., 2017; Oskin et al., 2017). We collected sediment from well-
257 shielded vertical or overhanging canyon walls, mostly within narrow canyons. In each case,
258 sediment was excavated from a horizontal depth of at least 50 cm into outcrops, parallel to bedding.
259 We sieved sediment in the field and collected the medium sand-sized fraction (250 – 500 μm). A
260 total of 15 samples were collected during this study; 13 samples were collected from outcrops, and
261 2 samples were collected from modern wash sediment at catchment outlets. Our goal was to
262 quantify both catchment-averaged paleodenudation in Pleasant Canyon through time, and to
263 quantify the modern catchment-averaged denudation rate.

264 Samples of Pleistocene and modern sediment underwent standard physical separation and
265 chemical purification procedures at the Purdue Rare Isotope Measurement Laboratory (PRIME
266 Lab). Samples were washed and wet sieved to remove fine particles, then underwent a technique
267 of froth-floatation to separate quartz from feldspar. Samples underwent magnetic separation and
268 were then treated with heavy liquids to isolate quartz. Purified quartz was then leached in dilute
269 HF-HNO₃ baths in an ultrasonic tank to remove the meteoric CRN components. All samples of
270 pure quartz were screened using inductively coupled plasma optical emission spectrometry (ICP-
271 OES). Samples of pure quartz were spiked with ²⁷Al or ⁹Be carrier of known concentration, and
272 dissolved using concentrated HF/HNO₃. Samples were then filtered through cation and anion
273 exchange columns, then Al and Be hydroxides were dried and converted to oxides, and loaded into
274 targets to be measured using accelerator mass spectrometry (AMS) at the PRIME Lab. AMS
275 results were corrected using blank concentrations following standard PRIME Lab procedures (See
276 “Supplementary AMS Data” file for complete chemistry blank and uncorrected sample
277 measurements).

278

279 3.3 Cosmogenic $^{26}\text{Al}/^{10}\text{Be}$ Burial Dating and Paleodenudation Calculations

280 Quartz sediment eroded from a catchment and mixed in a fluvial system retains a
281 concentration of CRNs (^{26}Al and ^{10}Be) inversely proportional to the spatially averaged denudation
282 rate within that catchment (Lal, 1991; Bierman and Steig, 1996; Granger and Muzikar, 2001).
283 Consequently, rapidly eroding landscapes result in low concentrations of CRNs in fluvial
284 sediment, while the opposite is true for slowly eroding landscapes. Sediment in catchment-fan
285 systems is evacuated and rapidly deposited on the fan surface, and assuming the pre-burial
286 concentration of CRN found in sediment is due to steady vertical advection during erosion, the
287 concentration ($N_{Al,Be}$ in atoms/g SiO_2) is simply a function of the erosion rate (E) in cm/yr:

288

$$289 \quad (1) N_{Al}(0) = \frac{A_0}{\frac{1}{\tau_{Al}} + \frac{E}{L_0}} + \frac{A_1}{\frac{1}{\tau_{Al}} + \frac{E}{L_1}} + \frac{A_2}{\frac{1}{\tau_{Al}} + \frac{E}{L_2}} + \frac{A_3}{\frac{1}{\tau_{Al}} + \frac{E}{L_3}}$$

290

$$291 \quad (2) N_{Be}(0) = \frac{B_0}{\frac{1}{\tau_{Be}} + \frac{E}{L_0}} + \frac{B_1}{\frac{1}{\tau_{Be}} + \frac{E}{L_1}} + \frac{B_2}{\frac{1}{\tau_{Be}} + \frac{E}{L_2}} + \frac{B_3}{\frac{1}{\tau_{Be}} + \frac{E}{L_3}}$$

292

293 Where A_j and B_j are coefficients, with values of $A_0 = 28.5$, $A_1 = 0.72$, $A_2 = 0.16$, $A_3 = 0.19$, $B_0 = 4$,
294 $B_1 = 0.09$, $B_2 = 0.02$, and $B_3 = 0.02$, and in units of atoms/yr/g SiO_2 , (Granger and Muzikar, 2001;
295 Borchers et al., 2016). L_j represents an attenuation length scale for CRN production reactions; L_0
296 refers to the attenuation length for spallogenic reactions, L_1 and L_2 are attenuation lengths for
297 negative muon capture, and L_3 is the attenuation length for fast muon capture. We assign values
298 of $L_0 = 160/\rho$, $L_1 = 738/\rho$, $L_2 = 2688/\rho$, and $L_3 = 4360/\rho$, where ρ represents rock density covering

299 a sample in g/cm³ (Granger and Muzikar, 2001). Density of overlying mass in the catchment during
 300 erosion is assumed to be 2.6 g/cm³, and the bulk density of sediment in the PCC is assumed to be
 301 2.2 g/cm³, and τ_{Al} and τ_{Be} represent the radioactive mean lives for ²⁶Al and ¹⁰Be (1.02x10⁶ and
 302 1.93x10⁶ yrs, respectively; Norris et al., 1983; Chmeleff et al., 2010).

303 Buried sediment derived from a steadily eroding source retains a concentration of CRNs
 304 that evolves through time as a function of the pre-burial concentration (itself a function of erosion
 305 rate), and the time since burial (Granger and Muzikar, 2001):

306

$$307 \quad (3) N_{Al}(t) = N_{Al}(0) \exp\left(\frac{-t}{\tau_{Al}}\right) + P_{Al}(d)\tau_{Al}[1 - \exp\left(\frac{-t}{\tau_{Al}}\right)]$$

308

$$309 \quad (4) N_{Be}(t) = N_{Be}(0) \exp\left(\frac{-t}{\tau_{Be}}\right) + P_{Be}(d)\tau_{Be}[1 - \exp\left(\frac{-t}{\tau_{Be}}\right)]$$

310

311 Where $N_{Al,Be}$ is the number of atoms/g SiO₂, t is time in years, $P_{Al,Be}$ are production rates in
 312 atoms/yr/g SiO₂, and d is sample depth in cm. In equations three and four, the first term describes
 313 post-burial radioactive decay, and the second term describes post-burial production of CRNs. At
 314 depths greater than several 10s of m, the right-hand term may be considered negligible, but post-
 315 burial production in shallowly buried sediment may be significant (Granger and Muzikar, 2001).
 316 Lacustrine environments such as pluvial lakes provide extra post-depositional shielding to
 317 sediment from cosmic rays, yet we elected to use an equation with terms that describe muonogenic
 318 post-burial CRN production:

319

$$320 \quad (5) P_{Al}(d) = A_0 \exp\left(\frac{-d}{L_0}\right) + A_1 \exp\left(\frac{-d}{L_1}\right) + A_2 \exp\left(\frac{-d}{L_2}\right) + A_3 \exp\left(\frac{-d}{L_3}\right)$$

321

322
$$(6) P_{Be}(d) = B_0 \exp\left(\frac{-d}{L_0}\right) + B_1 \exp\left(\frac{-d}{L_1}\right) + B_2 \exp\left(\frac{-d}{L_2}\right) + B_3 \exp\left(\frac{-d}{L_3}\right)$$

323

324 where A and B are mechanisms of CRN production as given in equations one and two. Equations
325 one through six combine through substitution to form a system of two equations and two
326 unknowns, time (t) and erosion rate (E), and using measured CRN concentrations ($N_{Al,Be}$) and the
327 depth of each sample (d), we may solve for both t and E . To recover t and E , we forward model
328 pre-burial concentrations of CRNs, and use a least-squares optimization to determine a best-fit
329 burial age and denudation rate for each measured pair of CRN concentrations (after Craddock et
330 al., 2010). We used published sea-level high latitude reference production rates for ^{26}Al and ^{10}Be
331 of 28.5 and 4 atoms/g SiO_2/yr , respectively (Borchers et al., 2016), and scaled them to the
332 catchment average production rates using latitude and catchment hypsometry to correct for altitude
333 and shielding by the horizon, resulting in catchment average production rates for ^{26}Al and ^{10}Be of
334 102 and 14.3 atoms/yr/g SiO_2 , respectively (Stone, 2000; and code described in Dortch et al.,
335 2011).

336

337 **3.4 Assumptions Associated with Burial Age and Paleodenudation Rate Calculations**

338 To calculate the $^{26}\text{Al}/^{10}\text{Be}$ burial age and paleodenudation rate from sediment in the PCC
339 we assumed the sampled bed was instantaneously buried to the modern depth below the fan surface
340 (~500 m asl). In reality, deposits aggraded by accumulation on the alluvial-fan surface and rapid
341 tectonically controlled subsidence of the hanging wall. A conservative estimate for the average
342 aggradation rate in the PCC is at least ~100 – 400 m/Ma (Vogel et al., 2002). Craddock et al.
343 (2010) calculated burial ages and denudation rates using an instantaneous emplacement model,

344 and again using a depth-dependent model; they found calculating burial ages and denudation rates
345 using the instantaneous emplacement model only resulted in significant bias when aggradation
346 rates were very low, on the order of 10 m/Ma, which is an order of magnitude lower than our
347 lowest estimate of aggradation rate.

348 We assumed a uniform distribution of quartz-bearing lithology in the catchment, and we
349 made no corrections for recent exposure to cosmic rays during exhumation, because (1) we have
350 no way to constrain the timing and rate of headward erosion in the PCC, except that incision
351 occurred after deposition of the youngest strata, and (2) we feel the measures taken during
352 sampling, as outlined in section 3.2, ensure samples were relatively well-shielded from modern
353 exposure. Reported errors for burial ages and denudation rates represent analytical uncertainties
354 and decay rate related uncertainties (See Table 1).

355

356 **4.0 RESULTS**

357 **4.1 Depositional Lithofacies Associations of the Pleasant Canyon Complex**

358 We used data from measured lithostratigraphic sections to construct depositional
359 lithofacies and lithofacies associations for stratigraphic units in the PCC (after Blair and
360 McPherson, 2008). Example lithofacies and lithofacies associations are pictured in Figure 4, and
361 the large-scale stacking patterns of facies associations are presented in Figure 5 (See
362 Supplementary material S2 for complete description).

363 Lithofacies of the PCC fall under one of two broad groups of depositional environments,
364 those deposited in or modified by subaqueous lacustrine environments during pluvial intervals
365 termed the Lacustrine Lithofacies Association, or those deposited on a subaerial alluvial fan
366 surface termed the Alluvial Lithofacies Association (after Blair and McPherson, 2008). In addition,

367 we note the occurrence of both Lacustrine and Alluvial Lithofacies in close vertical association,
368 which we call a Mixed Lithofacies Association.

369

370 ***4.1.1 Lacustrine (and Mixed) Lithofacies Association***

371 The Lacustrine Lithofacies Association (Fig. 4c – l) is defined by laterally continuous grey-
372 to white-colored, finely laminated to featureless beds of clay, silt, and sand. In Section One, several
373 meters of rhythmically bedded sandy turbidites are preserved (Fig. 4h). Characteristic lithofacies
374 that define the Lacustrine (and Mixed) Lithofacies Association include Lithofacies F: Fine silt to
375 clay (Fig. 4c – 4i), Lithofacies Gcr: rounded, clast-supported gravel conglomerate (not pictured),
376 and Lithofacies Sc: horizontally laminated and contorted sand beds (Fig. 4h).

377 The ‘mixed’ aspect of this lithofacies association refers to lithofacies (Fig. 4a, b, & l) that
378 are interpreted as distinct environments of deposition, alluvial and lacustrine, which are stacked in
379 close vertical succession, thus representing a mixed association. Where fine-grained units
380 interpreted as lacustrine (F, Sl) are interbedded with sands (Sl, Sg), and coarse-grained gravel
381 conglomerates (Gc, Gm), we interpret a shallow or ephemeral lake with rapidly fluctuating water
382 level or environment of deposition (examples pictured in Figure 4a, 4b, and in the upper 1/3 of
383 Figure 4k, and 4i).

384

385 ***4.1.2 Alluvial Lithofacies Association***

386 Alluvial fan facies are ubiquitous within the PCC, and are like those described in numerous
387 publications (*e.g.* Blair and McPherson, 2008). In the PCC, these facies are composed primarily
388 of cobble to boulder conglomerates interbedded with thin (cm) to thick (m) clean to muddy sand
389 beds of varying but typically low lateral continuity (Fig. 4m, n). Characteristic lithofacies that

390 define the Alluvial Lithofacies Association include Lithofacies Gm: matrix-supported gravel
391 conglomerate (Fig. 4m, n), Lithofacies Gc: clast-supported gravel conglomerate (Fig. 4m),
392 Lithofacies Sg: Granule-pebble rich sand (Fig. 4a), Lithofacies Sh: horizontally laminated or
393 featureless sand (Fig. 4a, d, h).

394

395 **4.2 Stratigraphic Architecture and Depositional Evolution of the PCC**

396 Here we use our scheme of lithofacies associations, and documented large-scale
397 stratigraphic architecture to describe the overall depositional history of the PCC (Fig. 5). Basal
398 deposits of the PCC indicate early deposition was dominated by coarse grained, muddy debris
399 flows, most likely on an alluvial fan surface, separated by laterally discontinuous and patchy
400 lacustrine-influenced conglomerate (minor lacustrine lithofacies; Gcr, Gc), as evidenced by clast
401 rounding, open framework, and relatively coarse matrix content.

402 Stratigraphically above the basal alluvial-fan dominated component of the PCC, the
403 sedimentological record shows a significant episode of system flooding, lake deepening, and
404 backstepping of coarse-grained lithofacies (positioned at ~115 – 120 m above base of Section Two,
405 and ~19 – 30 m above base of Section One; see Fig. 2c for locations of measured sections). The
406 Lacustrine Lithofacies Association at this interval (lithofacies F, and Sl) signals the greatest
407 relative water depth, and likely a major full glacial-pluvial climate event. Preservation of sandy
408 sediment gravity flows and meters of finely laminated silt to clay beds attest to deeper lake
409 conditions during this phase of PCC evolution.

410 Overlying the Lacustrine Lithofacies Association, we document a transition from
411 dominantly fine-grained deposits to thin sands, granule to pebbly sands, and muddy alluvial
412 sediments that prograde across fine grained facies, and grade laterally in the dip direction into

413 lacustrine facies. The mixed association of both alluvial and lacustrine lithofacies (Sl, Sg) grades
414 vertically into coarsening upward bundles of sand, pebble, and cobble to boulder conglomerate
415 (Sl, Sg, Gm, Gc). This evolution is likely in response to changes in base level associated with lake
416 desiccation.

417 We used the prominent lacustrine unit in the upper portion of the outcrop transect (Fig.5)
418 to correlate the two measured sections and to create a composite stratigraphic section for the PCC.
419 We note syndepositional normal faulting in the south part of the PCC, and subtle depositional
420 geometry of the paleo fan may explain the overall thickening, and lower stratigraphic position of
421 the lacustrine unit in Section One (See Supplementary Fig. 2.2).

422

423 **4.3 CRN-derived Stratigraphic Ages and Paleodenudation Rates**

424 Table 1 shows results of blank corrected AMS measurements, $^{26}\text{Al}/^{10}\text{Be}$ burial ages, and
425 paleodenudation rates for samples from modern catchment outlets and the PCC. Figure 6 shows
426 the global $\delta^{18}\text{O}$ curve (Lisiecki and Raymo, 2005) plotted with a synthesis of our stratigraphic and
427 CRN-derived data sets, including a composite stratigraphic section with sample locations,
428 interpreted lithofacies associations, CRN-derived burial ages, and CRN-derived paleodenudation
429 rates plotted against composite stratigraphic thickness.

430 The results of burial dating in the PCC yield a depositional age model that supports
431 previous interpretations for the age of basal stratigraphy of at least ca. 0.9 Ma (~20 m above the
432 playa floor; Vogel et al., 2002). However, our results indicate the PCC was an active alluvial fan
433 environment up to 0.6 Myr earlier than previously thought (Fig. 6). A basal burial age of ca. 1.55
434 \pm 0.22 Ma (PAN15), and a stratigraphically higher sample age of 1.16 \pm 0.25 Ma (PAN09) obey
435 stratigraphic superposition, and samples generally become younger up-section (Fig. 6d). Within
436 the composite stratigraphic section, the highest $^{26}\text{Al}/^{10}\text{Be}$ burial ages are ca. 0.36 \pm 0.16 Ma

437 (PAN04) and 0.52 ± 0.20 Ma (PAN05; see Table 1 & Fig. 6a), and constrain the timing of fan
438 abandonment.

439 Middle Pleistocene sediment samples from the PCC yield paleodenudation rates of similar
440 magnitude to estimates made by others in Death and Panamint Valley (Frankel et al., 2007; Jayko,
441 2005). Paleodenudation rates vary from 28 ± 4 mm/kyr (PAN01) up to 54 ± 10 mm/kyr (PAN13),
442 with a long term mean denudation rate for the PCC of 36 ± 8 mm/kyr (1σ for all PCC CRN-derived
443 paleodenudation rates; see Table 1). Modern sediment from Pleasant Canyon and Middle Park
444 Canyon outlets yields lower denudation rates of 24 ± 1 (PAN10) and 28 ± 2 mm/kyr (PAN12),
445 respectively, averaged over ca. 21 – 25 kyr timescales.

446 The highest measured paleodenudation rate, 54 mm/kyr, represents a $>2x$ increase (125%)
447 over the modern, and lowest rate of 24 mm/kyr for Pleasant Canyon. Individual paleodenudation
448 rates have uncertainties that do not overlap (Fig. 6), and while only 2/15 samples (13%) have errors
449 that fall outside the mean paleodenudation rate envelope, we note the highest and lowest CRN-
450 derived denudation rates vary by +50%/-33% from the long-term mean rate. In the remaining
451 sections, we focus on interpretation of these results, then discuss limitations to the methods, and
452 finally explore potential alternative drivers of CRN-derived denudation rate and sediment flux
453 variability in catchment-fan systems.

454

455 **5.0 DISCUSSION**

456 **5.1 Climate-driven Variability in Catchment-fan System Response**

457 Our primary objective was to explore how climate transitions affect the magnitudes and
458 temporal variability of CRN-derived signals of catchment denudation and sediment flux in a
459 natural unglaciated system. Paleodenudation rates in the PCC were not constant, though many

460 rates were similar in magnitude for much of >1 Myr interval. Modern denudation rates from
461 Pleasant and Middle Park Canyons (24 and 28 mm/kyr, respectively) are systematically lower than
462 all but one paleodenudation rate from the PCC (see Table 1), suggesting differences in sediment
463 transport rates or process regimes between Pleistocene and Holocene epochs. These results are
464 consistent with independent findings based on physical sedimentology of alluvial fans in Death
465 Valley (D'Arcy et al., 2016). Prolonged extreme aridity represents the most likely driver for the
466 observed decrease in CRN-derived denudation rates measured in modern samples.

467 Taken at face value, CRN-derived paleodenudation rates preserved in alluvial fan
468 stratigraphy have varied by a factor of ~2x. A pattern of relatively steady paleodenudation rates
469 juxtaposed with significant variability in the high end, as measured in the PCC, is similar to the
470 pattern of imposed erosion rates vs. resulting CRN-derived erosion rates simulated in Figure 1c.
471 This qualitative comparison between a predicted pattern of climate-driven actual erosion vs. CRN-
472 derived erosion (Fig. 1c) and our empirical record of CRN-derived denudation rate variability (Fig.
473 6e), and documented stratigraphic evidence for major environmental changes in Panamint Valley
474 (Figs. 5 & 6), suggests that glacial-interglacial climate transitions have an observable effect on
475 CRN-derived denudation rates and sediment flux in unglaciated catchment-fan systems.

476 We observe variability in depositional environments and CRN-derived paleodenudation
477 rates in sediments deposited after the middle Pleistocene transition. Though we cannot rule out
478 CRN-derived denudation rate variability during the early Pleistocene, as preserved in the sparsely
479 sampled lower portion of the PCC, we may compare our record to other CRN-derived
480 paleodenudation records measured across climate transitions in unglaciated catchments. Climate
481 cooling and increased variability across the Plio-Pleistocene transition did not affect CRN-derived
482 paleodenudation rates in southern California or Kentucky, USA (Oskin et al., 2017; Granger et al.,

483 2001). However post-middle-Pleistocene CRN-derived paleodenudation rates from Fisher Valley,
484 Utah, between ca. 0.6 – 0.7 Ma, varied by as much as 2x, and are up to 2x higher than modern
485 rates (Balco and Stone, 2005). Periglacial processes in the Pacific Northwest United States lead to
486 increased CRN-derived denudation rates during the last glacial maximum compared to the
487 Holocene (Marshall et al., 2015), and interglacial climates increased CRN-derived denudation
488 rates via enhanced chemical weathering in unglaciated catchments on the Texas Gulf Coast (Hidy
489 et al., 2014). Others have documented major changes in sedimentary processes regimes across
490 multi-millennial timescale climate transitions that produced measurable variability in CRN
491 concentrations (*e.g.* Garcin, et al., 2017).

492 Thus two tentative and related hypotheses may be drawn that explain observations from
493 the PCC and from published literature: (1) 100 kyr Milankovitch periods are more efficient than
494 41 kyr periods at modulating sediment flux, and thus CRN concentrations in unglaciated systems,
495 and (2) that variability in CRN-derived denudation rates is potentially the result of changes in
496 process regimes, rather than steady state erosion rates, across climate transitions. These hypotheses
497 make testable predictions and represent opportunities for future research related to climate-surface
498 dynamics.

499

500 **5.2 Limitations to Interpretation of CRN-derived Signals from Alluvial Fan Stratigraphy**

501 Changes in measured CRN-derived denudation and sediment supply apparent in our record
502 allude to catchment response to climate change. However, we acknowledge that several limitations
503 of the CRN methodology pose challenges to assessing the true magnitude and variability of
504 paleodenudation/sediment flux signals emitted from Pleasant Canyon. First, we note that alluvial
505 fans may experience allogenic or autogenic driven erosion-deposition processes, introducing

506 potential stratigraphic incompleteness and/or preferential stratal preservation (Armitage et al.,
507 2011; D'Arcy et al., 2016; Straub and Esposito, 2013). A second challenge relates to theoretical
508 constraints on the CRN technique. True denudation rates may only be measured using CRNs where
509 steady state between catchment erosion and CRN flux has been reached (Bierman and Steig, 1996).
510 In the context of Milankovitch climate forcing, a catchment's CRN export may never equilibrate
511 to the true denudation rate/sediment flux, especially during punctuated climate events (Fig. 1c).
512 As a result, CRN-derived denudation signals extracted from alluvial stratigraphy may be out of
513 phase and dampened compared to actual denudation/sediment flux. Last, it is plausible that the
514 resolution of sampling for this study does not capture other periods of high or low
515 paleodenudation/sediment supply that were recorded in alluvial stratigraphy (as in the lower
516 portion of the PCC, *e.g.* Fig. 6).

517 Potential stratigraphic incompleteness, long CRN lag times, and sample resolution limit
518 definitive interpretations of our data set. However, normal-fault bound, rapidly subsiding alluvial
519 basins likely represent the most complete archives of past continental surface dynamics (Straub
520 and Esposito, 2013), highlighting the value of these data. Furthermore, long CRN lag times may
521 suggest that our highest CRN-derived rates actually represent minimum estimates for true
522 denudation rates. In other words, it is likely that catchment-fans experience buffering or
523 dampening of the CRN-derived signal of climate-forced sediment flux (as in Fig. 1c). We propose
524 that future studies utilizing valuable alluvial fan records should consider potential stratigraphic
525 completeness and sample resolution as first order controls on robust data interpretation.

526

527 **5.3 Unsteady Catchment Processes and Denudation Signal vs. Noise**

528 It remains challenging to relate changes in apparent sediment transfer to specific external
529 forcings, even in well-constrained natural systems (*e.g.* Balco and Stone, 2005). Here, we consider
530 the potential for noise in the record, which we define as variability driven by up-system non-
531 equilibrium processes, *e.g.* complex sediment storage and remobilization or mass wasting in the
532 catchment. Consider two end-member scenarios: (1) thin (several m thick) and relatively old (>15
533 – 20 kyr since bedrock denudation) deposits stored within the upper catchment acquire a large
534 post-erosion CRN concentration, and when remobilized, become mixed with sediment of average
535 concentration, resulting in depressed apparent denudation rates, and (2) localized mass wasting
536 within the catchment supplies sediment with relatively low CRN concentrations, which when
537 mixed with sediment of average CRN concentration, results in an increase of apparent
538 paleodenudation rate. We prescribed plausible CRN concentrations to sediment from each scenario
539 — stored sediment or landslide-derived sediment — and applied a binary end-member mixing
540 model to estimate the relative contribution from each source necessary to drive variability equal
541 to the highest and lowest CRN-derived denudation rates from the PCC (See Supplementary
542 material S3 for complete explanation).

543 Figure 7 shows a conceptual illustration of processes that could impart noise in the
544 paleodenudation record, as well as the results of mixing high- and low-CRN concentration
545 sediment with average CRN concentration sediment. This analysis suggests that our lowest
546 denudation rate (24 mm/kyr) requires ~48% of sediment to be derived from a high-concentration,
547 recycled deposit, whereas the highest calculated paleodenudation rate (54 mm/kyr), requires ~56%
548 of sediment to be derived from a low-concentration source, presumably representing landslide-
549 derived material.

550 We observe no evidence in the upper catchment of significant fluvial incision and terrace
551 development that might be expected for $>10^4$ yr old deposits. Thus mixing of significant amounts
552 of old stored sediment (at least 48%) may be unlikely. In the case of the second scenario, mixing
553 of large proportions (~56%) of mass-wasting derived sediment is difficult to evaluate; the high-
554 relief and short length-scale of the system may suggest paleodenudation variability in the high end
555 could be driven by episodic mass wasting. Similar proportions (~50%) of landslide-derived
556 sediment were deduced from ^{10}Be concentrations found in some fluvial systems after widespread
557 coseismic landslides associated with the 2008 Wenchuan earthquake (West et al., 2014). Yet
558 another plausible scenario is that wetter, colder Pleistocene climates lead to enhanced rates of mass
559 wasting in the PCC (*e.g.* Marshall et al., 2015; D’Arcy et al., 2016). Detailed quantitative
560 sedimentological analyses could potentially help resolve these outstanding hypotheses. Still, our
561 analysis of catchment-fan sediment transfer through time and end-member sediment mixing
562 models represent a novel perspective on the role of climate transitions in modulating sedimentary
563 process regimes and catchment-fan sediment transfer.

564

565 **6.0 CONCLUSIONS**

566 We measured cosmogenic radionuclides (CRNs; ^{26}Al and ^{10}Be ; $n = 13$ samples) vertically
567 through a succession of outcropping Pleistocene alluvium, and in modern sediment ($n = 2$ samples)
568 from a linked catchment-fan system to examine the effects of climate change on magnitude and
569 temporal variability of CRN-derived denudation rates and source-to-sink sediment transfer. Full
570 glacial climates in the Panamint Valley region were $\sim 5 - 6$ °C colder, and the area experienced
571 $\sim 50 - 100\%$ more precipitation relative to the Holocene (D’Arcy et al., 2016, and references
572 therein), conditions that resulted in major pluvial lake formation in Panamint Valley as deduced

573 from lacustrine strata preserved in the Pleasant Canyon Complex (PCC). Many of the resultant
574 paleodenudation measurements from the PCC are similar in magnitude over the period of interest
575 (ca. 1.5 Ma through ca. 0.3 – 0.6 Ma), with a mean rate of 36 ± 8 mm/kyr (1σ). However,
576 paleodenudation and modern denudation rates do display maximum variability of +50%/-33%,
577 respectively, from the mean long-term denudation rate. Modern CRN-derived denudation in
578 Pleasant Canyon (24 ± 1 mm/kyr) is systematically lower than all Pleistocene paleodenudation
579 rates, suggesting climate plays a fundamental control on sedimentary process regimes in
580 catchment-fan systems. Simulated erosion-CRN concentration lag times suggest that the highest
581 measured CRN-derived paleodenudation rates (49 – 54 mm/kyr) from the PCC may represent
582 minimum estimates of true catchment paleodenudation. We explored other potential drivers of
583 denudation variability, specifically sediment recycling and sediment derived from localized
584 landslides in the catchment. An end-member mixing model suggests a proportion >50% of low-
585 CRN-concentration landslide-derived sediment is required to mix with average concentration
586 sediment to produce the highest denudation rates in our record. Sample age resolution prevents us
587 from delineating specific relationships between paleodenudation magnitude and specific
588 Milankovitch cycles — still, our paleodenudation record within a framework of documented
589 lithofacies associations preserved in the PCC depositional segment suggests the highest CRN-
590 derived paleodenudation rates occur in association with climatic transitions, *i.e.*, glacial-
591 interglacial cycles. CRN-derived paleodenudation rates are highest and most variable in samples
592 deposited after the middle Pleistocene transition — the change from 41 to 100 kyr periods —
593 suggesting that 100 kyr periodicity in climate forcing may result in significant changes in
594 sedimentary process rates and regimes within this, and other high-relief unglaciated catchment-
595 fan systems globally.

596

597 **ACKNOWLEDGEMENTS**

598 Financial support was provided by an American Chemical Society-Petroleum Research Fund-
599 Doctoral New Investigator grant (#53553-DNI8) to BWR with additional analytical support from
600 a Seed Grant from the Purdue Rare Isotope Measurement Laboratory (PRIME Lab) to CM and
601 BWR. Two anonymous reviewers provided insightful and helpful reviews that significantly
602 improved the quality of this manuscript. James Spotila, William Craddock, and Andrew Cyr
603 provided helpful conversations and insightful feedback during the evolution of this work. Marek
604 Cichanski provided insight on the provenance of sediment in the PCC. Neal Auchter and Theodore
605 Them assisted with field work, and others from the Virginia Tech Sedimentary Systems Research
606 Group offered constructive feedback. BWR thanks Hannah Scherer for assistance in the field
607 during project inception. Ron Schott photographed the Pleasant Canyon complex in beautiful detail
608 (Figure 2). Gigapans may be found at:
609 <http://www.gigageology.org/Collections/PanamintValley.html>

610

611 **APPENDICES**

612 Supplementary material related to this article may be found online at...

613

614 **REFERENCES**

- 615 Albee, A.L., Labotka, T.C., Lanphere, M.A., McDowell, S.D., 1981. Geologic Map of the
616 Telescope Peak Quadrangle, California.
- 617 Allen, P.A., 2008. Time scales of tectonic landscapes and their sediment routing systems. Geol.
618 Soc. London, Spec. Publ. 296, 7–28. doi:10.1144/SP296.2

619 Allen, P.A., Densmore, A.L., 2000. Sediment flux from an uplifting fault block. *Basin Res.* 12,
620 367–380. doi:10.1046/j.1365-2117.2000.00135.x

621 Armitage, J.J., Duller, R. a., Whittaker, A.C., Allen, P. A., 2011. Transformation of tectonic and
622 climatic signals from source to sedimentary archive. *Nat. Geosci.* 4, 231–235.
623 doi:10.1038/ngeo1087

624 Balco, G., Stone, J.O.H., 2005. Measuring middle Pleistocene erosion rates with cosmic-ray-
625 produced nuclides in buried alluvial sediment, Fisher Valley, southeastern Utah. *Earth*
626 *Surf. Process. Landforms* 30, 1051–1067. doi:10.1002/esp.1262

627 Bidgoli, T.S., Amir, E., Walker, J.D., Stockli, D.F., Andrew, J.E., Caskey, S.J., 2015. Low-
628 temperature thermochronology of the Black and Panamint mountains, Death Valley,
629 California: Implications for geodynamic controls on Cenozoic intraplate strain.
630 *Lithosphere* 7, 473–480. doi:10.1130/L406.1

631 Bierman, P., Steig, E.J., 1996. Estimating Rates of Denudation Using Cosmogenic Isotope
632 Abundances in Sediment. *Earth Surf. Process. Landforms* 21, 125–139.
633 doi:10.1002/(SICI)1096-9837(199602)21:2<125::AID-ESP511>3.0.CO;2-8

634 Blair, T.C., Mcpherson, J.G., 2008. Quaternary sedimentology of the Rose Creek fan delta,
635 Walker Lake, Nevada, USA, and implications to fan-delta facies models. *Sedimentology*
636 55, 579–615. doi:10.1111/j.1365-3091.2007.00913.x

637 Borchers, B., Marrero, S., Balco, G., Caffee, M., Goehring, B., Lifton, N., Nishiizumi, K.,
638 Phillips, F., Schaefer, J., Stone, J., 2016. Geological calibration of spallation production
639 rates in the CRONUS-Earth project. *Quat. Geochronol.* 31, 188–198.
640 doi:10.1016/j.quageo.2015.01.009

641 Castellort, S., Van Den Driessche, J., 2003. How plausible are high-frequency sediment supply-
642 driven cycles in the stratigraphic record? *Sediment. Geol.* 157, 3–13. doi:10.1016/S0037-
643 0738(03)00066-6

644 Chmeleff, J., von Blanckenburg, F., Kossert, K., Jakob, D., 2010. Determination of the ^{10}Be half-
645 life by multicollector ICP-MS and liquid scintillation counting. *Nucl. Instruments*
646 *Methods Phys. Res. Sect. B Beam Interact. with Mater. Atoms* 268, 192–199.
647 doi:10.1016/j.nimb.2009.09.012

648 Cichanski, M., 2000. Low-angle, range-flank faults in the Panamint, Inyo, and Slate ranges,
649 California: Implications for recent tectonics of the Death Valley region. *Bull. Geol. Soc.*
650 *Am.* 112, 871–883. doi:10.1130/0016-7606(2000)112<871:LRFITP>2.0.CO;2

651 Covault, J.A., Romans, B.W., Graham, S.A., Fildani, A., and Hilley, G.E., 2011. Terrestrial
652 source to deep-sea sink sediment budgets at high and low sea levels: insights from
653 tectonically active southern California. *Geology* 39:619–622.

654 Craddock, W.H., Kirby, E., Harkins, N.W., Zhang, H., Shi, X., Liu, J., 2010. Rapid fluvial
655 incision along the Yellow River during headward basin integration. *Nat. Geosci.* 3, 209–
656 213. doi:10.1038/ngeo777

657 D’Arcy, M., Whittaker, A.C., Roda-Boluda, D.C., 2016. Measuring alluvial fan sensitivity to
658 past climate changes using a self-similarity approach to grain-size fining, Death Valley,
659 California. *Int. Assoc. Sedimentol. Spec. Publ.* doi:10.1111/sed.12308

660 Densmore, A.L., Anderson, R.S., 1997. Tectonic geomorphology of the Ash Hill fault, Panamint
661 Valley, California. *Basin Res.* 9, 53–63. doi:10.1046/j.1365-2117.1997.00028.x

662 Densmore, A.L., Gupta, S., Allen, P.A., Dawers, N.H., 2007. Transient landscapes at fault tips. *J.*
663 *Geophys. Res.: Earth Surface* 112, F03S08. doi:10.1029/2006JF000560

664 Dortch, J.M., Owen, L.A., Schoenbohm, L.M., Caffee, M.W., 2011. Asymmetrical erosion and
665 morphological development of the central Ladakh Range, northern India.
666 *Geomorphology* 135, 167–180. doi:10.1016/j.geomorph.2011.08.014

667 Frankel, K.L., Brantley, K.S., Dolan, J.F., Finkel, R.C., Klinger, R.E., Knott, J.R., Machette,
668 M.N., Owen, L.A., Phillips, F.M., Slate, J.L., Wernicke, B.P., 2007. Cosmogenic ^{10}Be
669 and ^{36}Cl geochronology of offset alluvial fans along the northern Death Valley fault zone:
670 Implications for transient strain in the eastern California shear zone. *J. Geophys. Res.*
671 *Solid Earth* 112, 1–18. doi:10.1029/2006JB004350

672 Garcin, Y., Schildgen, T.F., Torres Acosta, V., Melnick, D., Guillemoteau, J., Willenbring, J.,
673 Strecker, M.R., 2017. Short-lived increase in erosion during the African Humid Period:
674 Evidence from the northern Kenya Rift. *Earth Planet. Sci. Lett.* 459, 58–69.
675 doi:10.1016/j.epsl.2016.11.017

676 Glotzbach, C., Van Der Beek, P., Carcaillet, J., Delunel, R., 2013. Deciphering the driving forces
677 of erosion rates on millennial to million-year timescales in glacially impacted landscapes:
678 An example from the Western Alps. *J. Geophys. Res. Earth Surf.* 118, 1491–1515.
679 doi:10.1002/jgrf.20107

680 Granger, D.E., Fabel, D., Palmer, A.N., 2001. Pliocene - Pleistocene incision of the Green River,
681 Kentucky, determined from radioactive decay of cosmogenic ^{26}Al and ^{10}Be in Mammoth
682 Cave sediments. *Bull. Geol. Soc. Am.* 113, 825–836. doi:10.1130/0016-
683 7606(2001)113<0825:PPIOTG>2.0.CO;2

684 Granger, D.E., Muzikar, P.F., 2001. Dating sediment burial with in situ-produced cosmogenic
685 nuclides: Theory, techniques, and limitations. *Earth Planet. Sci. Lett.* 188, 269–281.
686 doi:10.1016/S0012-821X(01)00309-0

687 Granger, D.E., Schaller, M., 2014. Cosmogenic Nuclides and Erosion at the Watershed Scale.
688 Elements 10, 369–373. doi:10.2113/gselements.10.5.369

689 Gulick, S.P.S., Jaeger, J.M., Mix, A.C., Asahi, H., Bahlburg, H., Belanger, C.L., Berbel, G.B.B.,
690 Childress, L., Cowan, E., Drab, L., Forwick, M., Fukumura, A., Ge, S., Gupta, S., Kioka,
691 A., Konno, S., LeVay, L.J., März, C., Matsuzaki, K.M., McClymont, E.L., Moy, C.,
692 Müller, J., Nakamura, A., Ojima, T., Ribeiro, F.R., Ridgway, K.D., Romero, O.E., Slagle,
693 A.L., Stoner, J.S., St-Onge, G., Suto, I., Walczak, M.D., Worthington, L.L., Bailey, I.,
694 Enkelmann, E., Reece, R., Swartz, J.M., 2015. Mid-Pleistocene climate transition drives
695 net mass loss from rapidly uplifting St. Elias Mountains, Alaska. Proc. Natl. Acad. Sci.
696 1–6. doi:10.1073/pnas.1512549112

697 Hidy, A.J., Gosse, J.C., Blum, M.D., Gibling, M.R., 2014. Glacial–interglacial variation in
698 denudation rates from interior Texas, USA, established with cosmogenic nuclides. Earth
699 Planet. Sci. Lett. 390, 209–221. doi:10.1016/j.epsl.2014.01.011

700 Jannik, N.O., Phillips, F.M., Smith, G.I., Elmore, D., 1991. A ³⁶Cl chronology of lacustrine
701 sedimentation in the Pleistocene Owens River system. Geol. Soc. Am. Bull. 103, 1146–
702 1159. doi:10.1130/0016-7606(1991)103<1146:ACCOLS>2.3.CO;2

703 Jayko, A.S., 2005. Late Quaternary denudation, Death and Panamint Valleys, eastern California.
704 Earth-Science Rev. 73, 271–289. doi:10.1016/j.earscirev.2005.04.009

705 Jerolmack, D.J., Paola, C., 2010. Shredding of environmental signals by sediment transport.
706 Geophys. Res. Lett. 37, 1–5. doi:10.1029/2010GL044638

707 Lal, D., 1991. Cosmic ray labeling of erosion surfaces: in situ nuclide production rates and
708 erosion models. Earth Planet. Sci. Lett. 104, 424–439. doi:10.1016/0012-
709 821X(91)90220-C

710 Marshall, J.A., Roering, J.J., Bartlein, P.J., Gavin, D.G., Granger, D.E., Rempel, A.W.,
711 Praskievicz, S.J., Hales, T.C., 2015. Frost for the trees: Did climate increase erosion in
712 unglaciated landscapes during the late Pleistocene? *Sci. Adv.* 1, e1500715–e1500715.
713 doi:10.1126/sciadv.1500715

714 Mason, C.C., Fildani, A., Gerber, T., Blum, M.D., Clark, J.D., Dykstra, M., 2017. Climatic and
715 anthropogenic influences on sediment mixing in the Mississippi source-to-sink system
716 using detrital zircons: Late Pleistocene to recent. *Earth Planet. Sci. Lett.* 466, 70–79.
717 doi:10.1016/j.epsl.2017.03.001

718 Nishiizumi, K., Imamura, M., Caffee, M.W., Southon, J.R., Finkel, R.C., McAninch, J., 2007.
719 Absolute calibration of ^{10}Be AMS standards. *Nucl. Instruments Methods Phys. Res. Sect.*
720 *B Beam Interact. with Mater. Atoms* 258, 403–413. doi:10.1016/j.nimb.2007.01.297

721 Norris, T.L., Gancarz, A.J., Rokop, D.J., Thomas, K.W., 1983. Half-life of ^{26}Al . *J. Geophys.*
722 *Res.: Solid Earth* 88, B331. doi:10.1029/JB088iS01p0B331

723 Oskin, M.E., Longinotti, N.E., Peryam, T., Dorsey, B., DeBoer, C., Housen, B., Blisniuk, K.,
724 2017. Steady ^{10}Be -derived paleo-erosion rates across the Plio-Pleistocene climate
725 transition, Fish Creek-Vallecito basin, California. *J. Geophys. Res. Earth Surf.*
726 doi:10.1002/2016JF004113

727 Oster, J.L., Ibarra, D.E., Winnick, M.J., Maher, K., 2015. Steering of westerly storms over
728 western North America at the Last Glacial Maximum. *Nat. Geosci.* 8, 201–205.
729 doi:10.1038/ngeo2365

730 Oswald, J.A., Wesnousky, S.G., 2002. Neotectonics and quaternary geology of the Hunter
731 Mountain fault zone and Saline Valley region, Southeastern California. *Geomorphology*
732 42, 255–278. doi:10.1016/S0169-555X(01)00089-7

733 Paola, C., Heller, P.L., Angevine, C.L., 1992. The large scale dynamics of grain size variation in
734 alluvial basins, 1: Theory. *Basin Res.* doi:10.1111/j.1365-2117.1992.tb00145.x

735 Phillips, F.M., 2008. Geological and hydrological history of the paleo – Owens River drainage
736 since the late Miocene, *Geological Soc. of America Special Publications* 2439, 1–36.
737 doi:10.1130/2008.2439(06).

738 Puchol, N., Charreau, J., Blard, P.H., Lavé, J., Dominguez, S., Pik, R., Saint-Carlier, D., Team,
739 A., 2017. Limited impact of quaternary glaciations on denudation rates in central Asia.
740 *Bull. Geol. Soc. Am.* 129, 479–499. doi:10.1130/B31475.1

741 Lisiecki, L.E., Raymo, M.E., 2005. A Pliocene-Pleistocene stack of 57 globally distributed
742 benthic δ 18O records. *Paleoceanography* 20, 1–17. doi:10.1029/2004PA001071

743 Romans, B.W., Castelltort, S., Covault, J.A., Fildani, A., Walsh, J.P., 2016. Environmental
744 signal propagation in sedimentary systems across timescales. *Earth-Science Rev.* 153, 7–
745 29. doi:10.1016/j.earscirev.2015.07.012

746 Smith, R.S.U., 1976. Late Quaternary Pluvial and Tectonic History of Panamint Valley, Inyo and
747 San Bernardino Counties, California. California Institute of Technology.

748 Snyder, N.P., Hodges, K. V., 2000. Depositional and tectonic evolution of a supradetachment
749 basin: $^{40}\text{Ar}/^{39}\text{Ar}$ geochronology of the Nova Formation, Panamint Range, California.
750 *Basin Res.* 12, 19–30. doi:10.1046/j.1365-2117.2000.00108.x

751 Stock, G.M., Anderson, R.S., Finkel, R.C., 2005. Rates of erosion and topographic evolution of
752 the Sierra Nevada, California, inferred from cosmogenic ^{26}Al and ^{10}Be concentrations.
753 *Earth Surf. Process. Landforms* 30, 985–1006. doi:10.1002/esp.1258

754 Stone, J.O., 2000. Air pressure and cosmogenic isotope production. *J. Geophys. Res. Solid Earth*
755 105, 23753–23759. doi:10.1029/2000JB900181

756 Straub, K.M., Esposito, C., 2014. Influence of Water and Sediment Supply on the Completeness
757 of the Stratigraphic Record and the Construction of Stratigraphic Surfaces in Alluvial
758 Fans and Deltas. *Journal of Geophysical Research: Earth Surface*, 118, 625–637,
759 doi:10.1002/jgrf.20061

760 Vogel, M.B., Jayko, A.S., Wooden, J.L., Smith, R.S.U., 2002. Quaternary exhumation rate
761 Central Panamint Range, California from U–Pb Zircon Ages. *Abstracts with Programs*,
762 Geological Society of America 34, 249.

763 West, A. J., R. Hetzel, G. Li, Z. Jin, F. Zhang, R. G. Hilton, and A. L. Densmore (2014),
764 Dilution of ^{10}Be in detrital quartz by earthquake-induced landslides?: Implications for
765 determining denudation rates and potential to provide insights into landslide sediment
766 dynamics, *Earth Planet. Sci. Lett.*, 396, 143-153, doi:10.1016/j.epsl.2014.03.058.

767

768 **FIGURE CAPTIONS**

769

770 **Figure 1:** Modeled changes in sediment flux (q_s per unit width) and erosion rate across two
771 timescales (Myr and kyr), resulting from perturbations in climatic or tectonic boundary
772 conditions in a catchment-fan system bounded by a range-front normal fault, and simulated
773 imposed erosion rate plotted with resultant CRN-derived erosion rate. Time progresses from left
774 to right in all plots. **a:** q_s response to stepwise increase (+100%, black line) or decrease (-50%,
775 gray line) in precipitation rate. **b:** q_s response to stepwise increase (+100%, black line) or
776 decrease (-50%, gray line) in fault slip rate. Dashed vertical red line indicates timing of change in
777 forcing in parts a and b. Modified from Densmore et al. (2007). **c:** Simulated response of
778 cosmogenic radionuclide (CRN) derived erosion rates to a change in actual (imposed) erosion

779 rate. The duration of the simulation is similar to that of middle to late Pleistocene Milankovitch
780 periods of 100 kyrs. Green solid line represents user defined erosion rate, and blue dashed line
781 represents the model output, or CRN-derived erosion rate through time. ^{10}Be production rate for
782 simulation as described in main text and code described in Garcin et al. (2017).

783

784

785 **Figure 2:** Study area shaded relief map, regional paleoclimatic reconstruction, and photopanorama
786 of the Pleasant Canyon Complex (PCC). **a:** Topography, and active faults of the Panamint/Death
787 Valley area. Pleasant Canyon catchment-fan system highlighted in red dashed lines. Extents of
788 Pleistocene pluvial lakes of the Owens River system highlighted in dashed blue lines, and blue
789 arrows denote pluvial lake flow directions into and out of Panamint Valley (Reheis et al., 2014).
790 **b:** Last glacial maximum paleoclimatic reconstruction showing precipitation change for the
791 western United States after Oster et al. (2015). **c:** Photopanorama of the PCC with locations of
792 measured sections (Photo credit: Ron Schott). AHFZ = Ash Hill fault zone, Mid. Park = Middle
793 Park Canyon, PEDF = Panamint Emigrant detachment fault, PVFZ = Panamint Valley fault zone.
794 Fault data from U.S. Geological Survey Quaternary fault database. 1 arc second elevation data
795 from the U.S. Geological Survey.

796

797

798 **Figure 3:** Pleasant Canyon catchment metrics. **a:** digital elevation model. **b:** Surface slope map.
799 **c:** Areal distribution of lithology in the catchment. All units are quartz bearing except for the
800 Sentinel Peak dolomite and probably the basalt/amphibolite unit (after Albee et al., 1981). **d:**
801 Pleasant Canyon catchment hypsometry. Left y-axis represents total catchment area within each

802 bin, x-axis represents elevation of catchment increasing from left to right (100 equal bins, each
803 22.7 m), and right y-axis is the cumulative catchment area. 1 arc second elevation data from U.S.
804 Geological Survey.

805

806

807 **Figure 4:** Lithofacies of the Pleasant Canyon complex. **a, b:** Horizontally laminated and low-angle
808 cross-stratified sand and granule- to pebble-rich beds (lithofacies Sl, Sg) that compose a
809 gradational transition in lithofacies from Lacustrine Lithofacies Association to Alluvial
810 Lithofacies Association. Note thick gravel debris flow capping units in **b** (lithofacies Gc, Gm). **c**
811 – **l:** dominantly fine-grained silt and clay (lithofacies F, Sl, Sg) that composes the Lacustrine
812 Lithofacies Association. **c:** Pebble-granule-rich sand lithofacies (Sg). **d:** Laminated sand
813 lithofacies (Sl). **e, f:** Fine-grained and pebble-granule rich lithofacies (Sf, Sg, and F), with small
814 burrows or root-traces. **g:** interbedded fine-grained and granule-rich lithofacies (F, Sg). **h:** Sandy
815 turbidites with contorted bedding (Sl). **i:** Laminated to cross-laminated sand with weakly
816 developed paleosol (Sl). **j:** fine grained lacustrine lithofacies (F) with possible varves. **k:** Thick
817 exposure (note person for scale) of fine-grained lithofacies (F, Sl) composing the Lacustrine
818 Lithofacies Association in section one. **l:** Interbedded fine-grained and gravel lithofacies (F, Gm,
819 Gc) that compose the Lacustrine (and Mixed) Lithofacies Association in Section Two. **m, n:**
820 Interbedded clast- and matrix-supported debris flow gravels with lenticular to laterally continuous
821 sands (lithofacies Gc, Gm, Sl, Sf) typical of the Alluvial Lithofacies Association.

822

823

824 **Figure 5:** Photomosaics and large-scale lithofacies associations and stratigraphic architecture of
825 the Pleasant Canyon Complex (PCC). **a:** Uninterpreted photomosaic of the southwest PCC. **b:**
826 interpreted photomosaic from part a, with colored lithofacies associations. **c:** Uninterpreted
827 photomosaic of the northwest PCC with the ghost town of Ballarat in the foreground. **d:** Interpreted
828 panel from part c illustrating subtle inclined geometries of progradational foresets within alluvial-
829 lacustrine lithofacies. Lacustrine units pinch-out or grade into mixed or alluvial lithofacies
830 associations up dip.

831

832

833 **Figure 6a:** Overview of the Pleasant Canyon complex (PCC) with schematic locations of
834 measured lithostratigraphic sections and cosmogenic radionuclide (CRN) samples. **6b – e:**
835 Pleistocene paleoclimate, PCC composite stratigraphic framework, burial ages, and
836 paleodenudation rates since ca. 1.5 Ma. **b:** Global oxygen isotope curve of Lisiecki and Raymo,
837 (2005), with known pluvial lake events in Panamint Valley shaded blue (after Jannick et al.,
838 1991). **c:** Composite stratigraphic section with interpreted lithofacies associations and CRN
839 sample numbers and positions. Blue shaded boxes indicate stratigraphic position of Lacustrine
840 Lithofacies Associations. **d:** CRN-derived burial ages vs. composite stratigraphic height, **e:**
841 CRN-derived paleodenudation rates vs. composite stratigraphic height beginning at ca. 1500 kyr.
842 Dashed vertical lines are mean and standard deviation (1σ) of all paleodenudation rates. Modern
843 catchment denudation rates are plotted at 5 meters height and shown with red circles. Individual
844 sample error bars represent the average of upper and lower bounds (1σ) on burial age-erosion
845 rate calculations (after Craddock et al., 2010). Refer to text and Supplementary Materials for
846 explanation of composite stratigraphic framework.

847

848 **Figure 7:** Conceptual model and binary mixing model results. 7a: catchment-fan system with low
849 CRN-concentration (red) landslide derived material, and high CRN-concentration (blue)
850 stored/recycled material. 7b: Curves represent synthetic ^{10}Be -derived denudation rates associated
851 with a given mixture of either low CRN-concentration landslide-derived sediment (red curve), or
852 high CRN-concentration stored/recycled sediment (blue curve), with ‘average’ concentration
853 sediment that experienced a mean erosion rate of ~ 36 mm/kyr.

854

855

856

Table 1: Corrected AMS results, ^{26}Al and ^{10}Be burial ages and denudation rates for samples from the Pleasant Canyon Complex and modern catchment outlets, Panamint Range and Valley, USA

Sample location information						AMS Results (blank corrected)				Burial ages and denudation rates			
sample ID	lat.	lon.	elevation (m asl)	depth (cm)	location	^{26}Al (a/g SiO_2)	*error	^{10}Be (a/g SiO_2)	error	$^{26}\text{Al}/^{10}\text{Be}$ burial age (yr)	† error (yr)	denudation rate (mm/kyr)	error (mm/kyr)
PAN01	36.02861	-117.21487	430	7000	PCC	1309759	43805	252927	6311	705,000	155,000	28	4
PAN02	36.0293	-117.21377	466	3400	PCC	1564624	55644	263806	9493	425,000	176,000	31	5
PAN03	36.0293	-117.21377	466	3400	PCC	1564426	77465	262072	7548	410,000	192,000	31	5
PAN04	36.02942	-117.21354	476	2400	PCC	1103834	40630	177904	5627	359,000	175,000	49	7
PAN05	36.0295	-117.21344	481	1900	PCC	1214501	48460	209390	6973	518,000	200,000	39	6
PAN06	36.02905	-117.21461	435	6500	PCC	1258579	64415	218528	7525	486,000	205,000	36	6
PAN07	36.03671	-117.21848	482	1800	PCC	1600021	59776	256047	6211	326,000	158,000	34	4
PAN08	36.03579	-117.21942	452	4800	PCC	1046392	51235	195296	5617	654,000	199,000	37	6
PAN09	36.03536	-117.22203	366	13400	PCC	671949	33194	160023	7205	1,164,000	252,000	34	6
PAN10	36.04724	-117.21092	412	...	Modern Pleasant Canyon	2225616	77950	362733	8772	24	0.6
PAN11	36.03868	-117.2192	482	1800	PCC	1341444	57291	245223	11679	645,000	248,000	31	6
PAN12	36.02749	-117.21577	390	...	Modern Middle Park	1637336	65025	287452	16818	28	1.6
PAN13	36.03493	-117.21848	448	5200	PCC	755308	29065	137675	6190	618,000	211,000	54	10
PAN14	36.02861	-117.21487	430	7000	PCC	1210537	60013	215151	8287	536,000	212,000	36	7
PAN15	36.04103	-117.22286	336	16400	PCC	471472	20247	134163	4084	1,549,000	223,000	34	5

857 *AMS measurement errors based on one standard deviation of analytical uncertainties

858 †Burial ages/denudation rate errors include analytical uncertainty and decay rate uncertainties for $^{26}\text{Al}/^{10}\text{Be}$ (Norris et al., 1983; Chmeleff et al.,
859 2010).

860

861 **SUPPLEMENTARY MATERIALS**

862

863 **Supplementary Text S1.0, S2.0, S3.0, References**

864 **Supplementary Figures S1, S2.1, S2.2, S3**

865 **Supplementary Data File “Supplementary AMS Data”**

866

867 **S1.0 CLAST PROVENANCE OF THE PLEASANT CANYON COMPLEX**

868 Sediments preserved in deposits of the PCC were mainly derived from the Pleasant Canyon
869 catchment, as indicated by the position of the deposit at the canyon mouth, the progradation
870 direction of the PCC, a closed drainage in the upper portions of Middle Park catchment, and
871 sediment provenance (clast compositions) in measured sections. Pleasant Canyon contains a
872 unique geologic unit known as the World Beater complex, a foliated gneiss with well-developed
873 augen porphyroblasts (Albee et al., 1981). The World Beater is not present in the Middle Park
874 catchment; thus, the presence of World Beater clasts supports a model where sediment preserved
875 in the PCC was derived largely from the Pleasant Canyon. We conducted reconnaissance-level
876 field work to survey for the presence of this unique lithology in our measured lithostratigraphic
877 sections; clasts of World Beater were ubiquitous at all levels of strata in outcrop, and in float along
878 canyon floors, (Supplementary Figure 1). We are confident that sediment in the PCC was derived
879 from Pleasant Canyon, and that the use of a catchment average production rate derived from the
880 hypsometry of Pleasant Canyon is justified. We note Middle Park catchment probably contributed
881 minor amounts of sediment to the PCC, but the small difference in catchment hypsometry only

882 affects the production of CRNs to a minor degree (~ 1 atom/g SiO_2/yr) and thus we elect to use one
883 catchment production rate for all rate and age calculations for samples from outcrop in the PCC.

884

885 **S2.0 DEPOSITIONAL LITHOFACIES OF THE PLEASANT CANYON COMPLEX**

886 We used data from measured lithostratigraphic sections to construct depositional
887 lithofacies and lithofacies associations for units in the PCC (after Miall, 1985; Blair and
888 McPherson, 2008; Blair and McPherson, 2009). The following sections describe lithofacies
889 associations and their interpreted lithofacies components. Example lithofacies and lithofacies
890 associations are pictured in Figure 4, and the large-scale stacking patterns of lithofacies
891 associations are presented in Figure 5.

892

893 **S2.1 Alluvial Lithofacies Association**

894 Alluvial fan lithofacies are ubiquitous within the PCC, and are similar to those described
895 in previous publications (*e.g.* Blair and McPherson, 2009). In the PCC these lithofacies are
896 composed primarily of cobble to boulder conglomerates interbedded with thin clean to muddy
897 sand beds of varying lateral continuity (Figure 4m, n).

898

899 Lithofacies Gm: matrix supported gravel conglomerate

900 Lithofacies Gm is found throughout the PCC in continuous to laterally discontinuous beds
901 of 10 cm to >1 -3 m thickness. Gm matrix is brown to greyish green, sand- to silt-sized grains, with
902 pebble- to cobble- to boulder-sized angular to subangular clasts. Lithofacies Gm usually lacks
903 internal structure, but may contain faint stratification. Lithofacies Gm is interpreted to be the
904 product of pseudoplastic, unconfined to channelized mud-supported debris flows.

905

906 Lithofacies Gc: clast supported gravel conglomerate

907 Lithofacies Gc is found throughout the PCC, and is often laterally continuous to
908 discontinuous over 1s to 10s of meters, can be <10 cm to >3 m in thickness, is composed of angular
909 and subangular pebble to boulders, with interstitial sand- and silt-sized grains. Clasts may be
910 imbricated with evidence for bedload traction structures and faint stratification. Matrix in Gc is
911 typically fine to coarse sand with little mud present. Lithofacies Gc is interpreted to be water-lain
912 debris flow deposits, reworked debris-flow material, or sieve deposits. Gc is pictured in Figure
913 4m.

914

915 Lithofacies Sg: Granule-pebble rich sand

916 Lithofacies Sg occurs in the transition from fine-grained units to conglomerate alluvium in
917 Section One in the south PCC. Granule- to pebble-rich coarse to medium sand in beds 10 cm – >1
918 m thick are faintly laminated or contain low-angle cross stratification. Traction structures indicate
919 a water-lain origin, either subaerial or subaqueous deposition, while the association of these
920 lithofacies to fine-grained lithofacies (discussed below) indicates a possible shallow lacustrine
921 origin. Facies Sg is pictured in Figure 4a.

922

923 Lithofacies Sh: horizontally laminated or structureless sand

924 Lithofacies Sh is found throughout the PCC in laterally continuous to discontinuous beds
925 ranging from 1 cm up to 3 m thickness. Laminations of very fine to medium-upper sand may be
926 graded, or display load structures and deformation along bed contacts. Faintly bedded to
927 structureless sand may exist in association with laminated beds. Lithofacies Sh is interpreted to

928 represent unconfined sheetwash deposits in distal alluvial environment, possible waning stage
929 subaerial dilute sediment flows. Lithofacies Sh is pictured in Figure 4a, d, and h.

930

931 **S2.2 Lacustrine (and Mixed) Lithofacies Association**

932 The Lacustrine Lithofacies Association is defined by finely laminated to featureless beds
933 of fine silt to clay, and in section one, several meters of rhythmically bedded sandy turbidites.
934 Lithofacies Sh, F, and Sg are the most common facies in the Lacustrine Lithofacies Association,
935 and are pictured in Figure 4d – j.

936 Mixed lithofacies are present in both Alluvial and Lacustrine Lithofacies Associations, thus
937 the term Mixed Lithofacies does not refer to a specific depositional environment, but rather an
938 association of two mixed environments of deposition, stacked in vertical succession. Where fine-
939 grained units interpreted as lacustrine (F, Sl) are interbedded with sands (Sl, Sg), and coarse-
940 grained gravel conglomerates (Gc, Gm), we interpret a shallow or ephemeral lake with rapidly
941 fluctuating environment of deposition. Examples of the Mixed Lithofacies are pictured in Figure
942 4a, 4b, and in the upper 1/3 of Figure 4k, and 4i.

943

944 Lithofacies F: Fine silt to clay

945 Lithofacies F crops out in laterally-continuous (100s m to km) deposits across the PCC,
946 specifically in Section Two at ~115 – 119 m, and in Section One at ~19 – 28 m above the base of
947 sections. Lithofacies F contains CaCO_3 and reacts to HCl, is white or greyish green or yellow in
948 color, and composed of very fine sand, silt and clay-sized grains. sparse disarticulated ostracod or
949 gastropod(?) fossils are observed in thin section. Bedforms include mm to cm scale horizontal,
950 wavy, and crinkly lamination, minor ripple cross laminations, and reddish siderite filled root traces

951 or burrows. Lithofacies F is commonly interbedded with Gm, and grades into Sf, Sl, and Gc, Gm
952 up section. Lithofacies F is interpreted to represent a shallow to deep lacustrine environment. The
953 complexity of preserved bedforms and dominant grain size argues against deposition in a fluvial
954 or alluvial environment. Lithofacies F might best be termed a lacustrine marl.

955

956 Lithofacies Sc: horizontally laminated and contorted sand beds

957 Subaqueous sandy turbidity currents, stacked in sets of normally graded beds displaying
958 contorted laminae, or dewatering structures. Sandy turbidites are subaqueous deposits interpreted
959 to represent relatively deep lacustrine depositional environments. Lithofacies Sc is pictured in
960 Figure 4h.

961

962 Lithofacies Gcr: rounded clast supported gravel conglomerate

963 Lithofacies Gcr is found at only one location, in the base of Section One (southern PCC;
964 Figure 5). Gcr has the same sedimentary characteristics as Gc, with the notable difference of
965 abundant subrounded to rounded pebble to cobble clasts and little matrix or when present loose
966 coarse-grained sand and granule matrix. We interpret facies Gcr as wave reworked beach gravel
967 deposits. Modern gravels near catchment outlets are typically angular with little rounding of clasts.

968

969 **S3.0 SUPPLEMENTARY TEXT FOR MIXING MODEL**

970

971 **S3.1 Mixing model**

972 We used a simple two-component (binary) mixing model to estimate proportions of various
973 sediment sources necessary to drive observed CRN-derived paleodenudation variability. The CRN

974 concentration (^{10}Be) in a binary mixture is dependent upon the starting concentration of end
975 members ($C_{A,B}$) and the proportions of each end member present in a mixture (f_A):

976

$$(Eq.S1) C_m = C_A f_A + C_B (1 - f_A)$$

978

979 where C_m is the concentration of the binary mixture. We specified end-member concentrations
980 (explained below), mixed end members, and used the resulting ^{10}Be concentration of mixed
981 sediment, and the standard steady state catchment denudation equation (See Fig. 1 in Granger and
982 Schaller, 2014) to calculate a denudation rate associated with each calculated mixed value of C_m .
983 Supplementary Figure 3 shows the sensitivity of calculated denudation rate to prescribed end
984 member concentrations. Lower CRN concentrations represent landslide-derived sources, and
985 higher CRN concentrations represent stored sediment sources.

986

987 **S3.2 Justification for end member CRN concentrations used in mixing model**

988 The CRN-concentrations used in our mixture model were prescribed based on several
989 factors: (1) the value assigned to the ‘average’ sediment fraction is based on the mean
990 paleodenudation rate of the catchment, *i.e.* 36 mm/kyr, which corresponds to $\sim 2.5 \times 10^5$ atoms
991 $^{10}\text{Be}/\text{g SiO}_2$, (2) the value of the ‘stored sediment’ end member is twice the average concentration
992 (5×10^5 atom/g SiO_2), and was estimated using a beginning ‘average’ concentration for a theoretical
993 deposit, and assuming exposure for ~ 15 kyr near the surface at elevations of $\sim 1800 - 2000$ m asl,
994 where production rates range, but are approximately 16 atoms $^{10}\text{Be}/\text{g SiO}_2/\text{yr}$ (we do not consider
995 decay of ^{10}Be to be important at this timescale), and finally, (3) for the mass wasting-derived CRN
996 concentration, we assumed relatively shallow mass failures ($\sim 1 - 3$ m depths) that may entrain

997 other material such as pre-existing regolith and bedrock, and we assigned this end member a value
998 of 1×10^5 a/g SiO_2 . We acknowledge concentrations of mass wasting derived sediment may be
999 extremely variable and dependent on the depth of detachment (Yanites et al., 2009). We also
1000 acknowledge that the resultant proportions of stored or mass wasting derived sediment necessary
1001 to drive denudation variability are dependent upon the prescribed CRN concentrations.
1002 Supplementary Figure S3 shows the sensitivity of ^{10}Be -derived denudation rates associated with a
1003 range of end-member concentrations, and highlights the necessity for mixing of significant
1004 proportions (>35 – 45%) of any modeled end member sources with average concentration sediment
1005 to drive the magnitude of variability observed in the PCC.

1006

1007

1008 **References**

- 1009 Albee, A.L., Labotka, T.C., Lanphere, M.A., McDowell, S.D., 1981. Geologic Map of the
1010 Telescope Peak Quadrangle, California.
- 1011 Blair, T.C., McPherson, J.G., 2008. Quaternary sedimentology of the Rose Creek fan delta,
1012 Walker Lake, Nevada, USA, and implications to fan-delta facies models. *Sedimentology*
1013 55, 579–615. doi:10.1111/j.1365-3091.2007.00913.x
- 1014 Blair, T.C., McPherson, J.G., 2009. Processes and forms of alluvial fans, *Geomorphology of*
1015 *Desert Environments*. doi:10.1007/978-1-4020-5719-9_14
- 1016 Granger, D.E., Schaller, M., 2014. Cosmogenic Nuclides and Erosion at the Watershed Scale.
1017 *Elements* 10, 369–373. doi:10.2113/gselements.10.5.369
- 1018 Miall, A., 1985. Architectural-Element Analysis : A New Method of Facies Analysis Applied to
1019 Fluvial Deposits. *Earth Sci. Rev.* 22, 261–308.

1020

1021 **Supplementary Figure Captions**

1022

1023 **Supplementary Figure S1:** Clasts of augen gneiss (World Beater complex) unique to the Pleasant
1024 Canyon catchment are found throughout measured sections of the Pleasant Canyon complex, in
1025 float and *in situ* within outcrops. **a, b:** Well-formed feldspar augen porphyroblasts in clasts of
1026 World Beater found in float in section 1. **c, d:** Examples of World Beater clasts found in outcrop
1027 in section 1.

1028

1029 **Supplementary Figure S2.1:** Correlations of lithostratigraphic measured sections and
1030 cosmogenic radionuclide (CRN) sample location within the Pleasant Canyon complex (PCC). **a:**
1031 Photomosaic of outcrops of the PCC with CRN sample locations marked with red filled circles
1032 and associated text with sample numbers. White arrows denote samples taken from catchment
1033 outlets and modern CRN-derived denudation rates. **b:** Simplified lithostratigraphic sections one
1034 and two from the PCC with CRN results placed within stratigraphy.

1035

1036 **Supplementary Figure S2.2:** **a:** Syndepositional normal fault (~NW-SE striking) in north wall of
1037 Middle Park Canyon, approximately 200 m south of Section One. **b:** close up of three to five
1038 meters of throw on a steep normal fault (shown as dashed red line), down toward the basin in part
1039 S2.2a. Subsidence via active normal faulting in part explains the expanded lacustrine strata in the
1040 southern Pleasant Canyon complex.

1041

1042 **Supplementary Figure S3:** Sensitivity of calculated denudation rates to prescribed end member
1043 CRN concentrations and relative mixing proportions. Red curves show proportion of low-CRN
1044 concentration mass-wasting derived sediment of various concentrations required to produce
1045 highest denudation rate. Blue curves show proportion of high-CRN concentration stored/recycled
1046 sediment of various concentrations required to produce lowest denudation rate. Bold curves
1047 represent values used in the main text. Horizontal grey dashed lines are the measured maximum
1048 (54 mm/kyr) and minimum (24 mm/kyr) denudation rates for the Pleasant Canyon complex.
1049
1050
1051

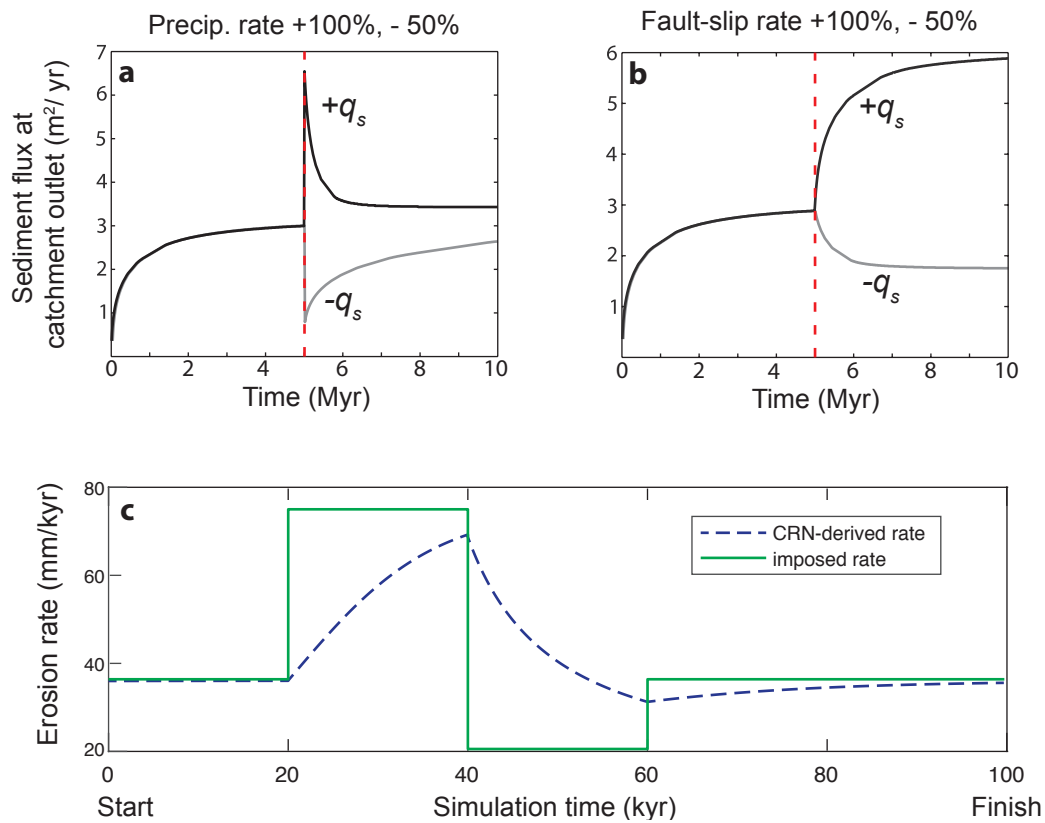


Figure 1

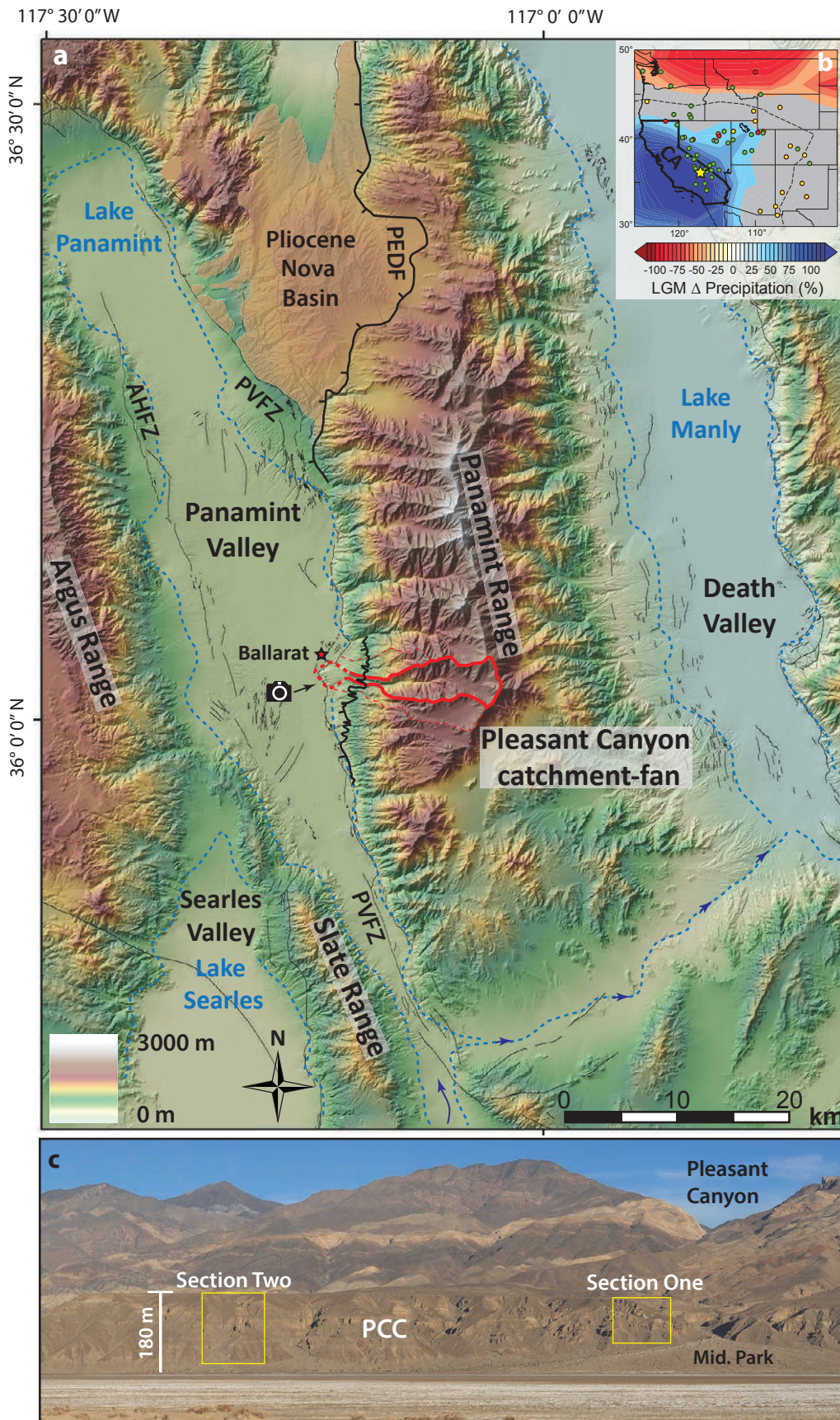


Figure 2

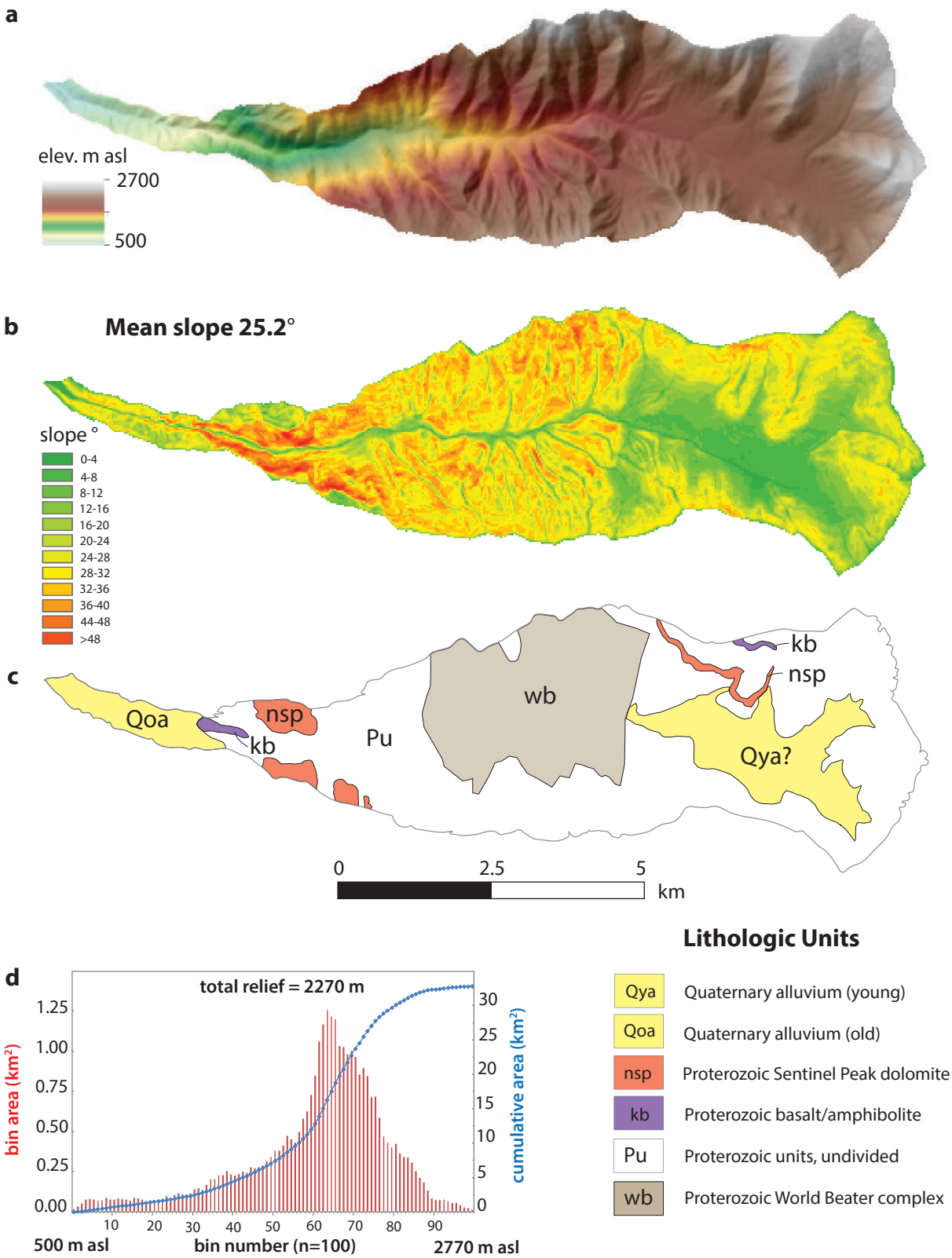


Figure 3

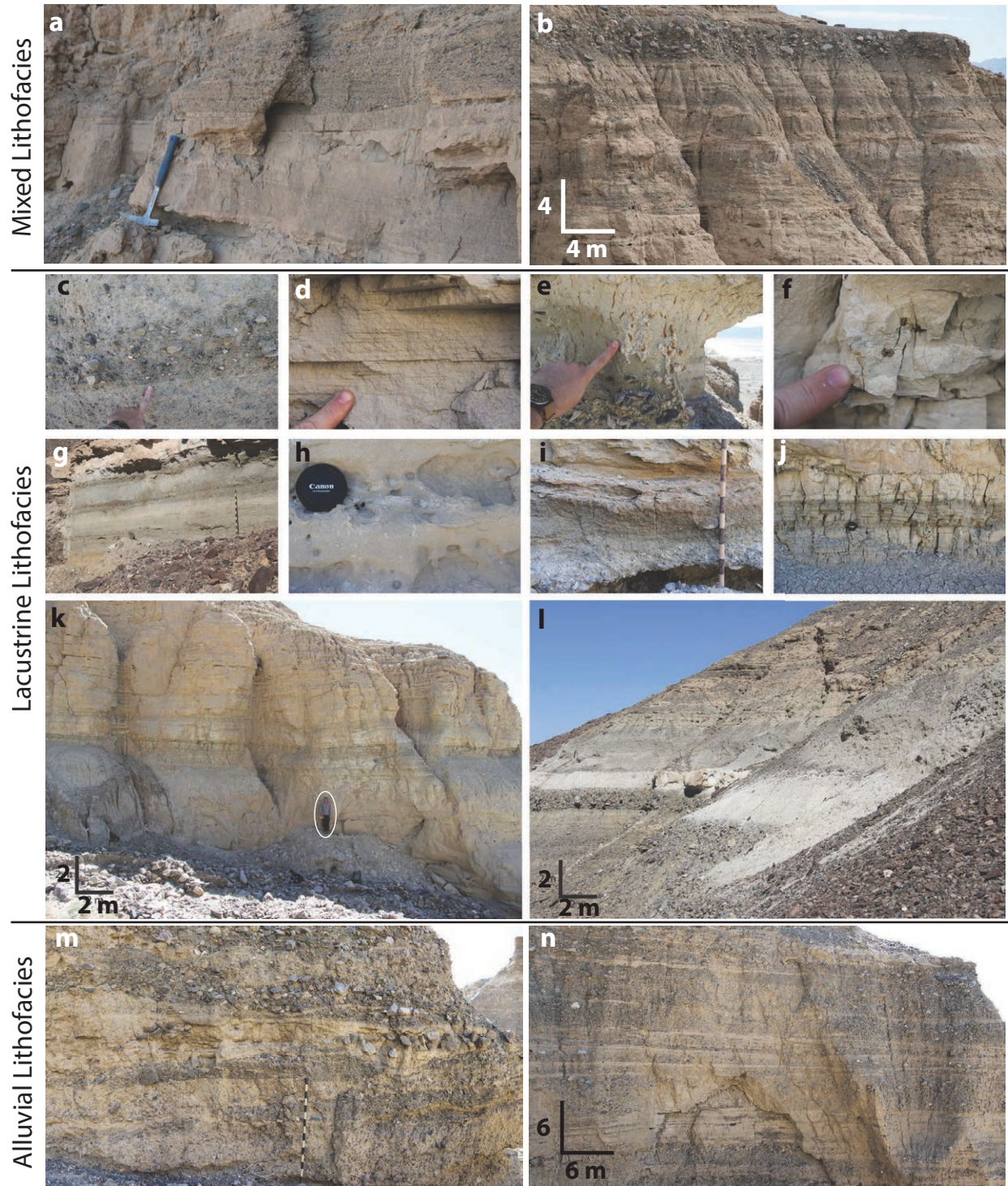


Figure 4

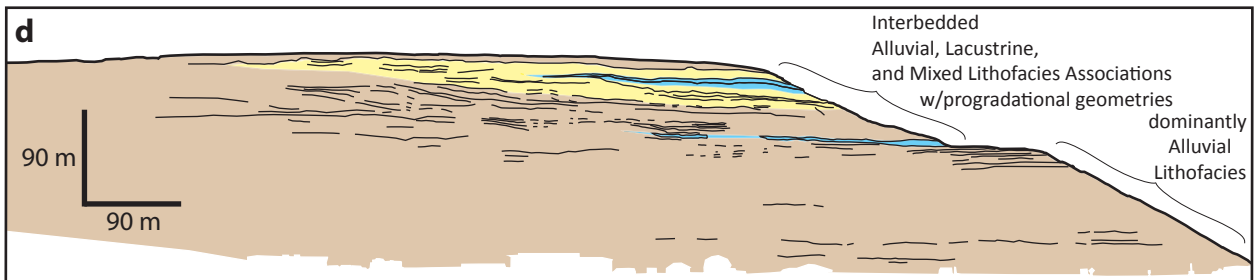
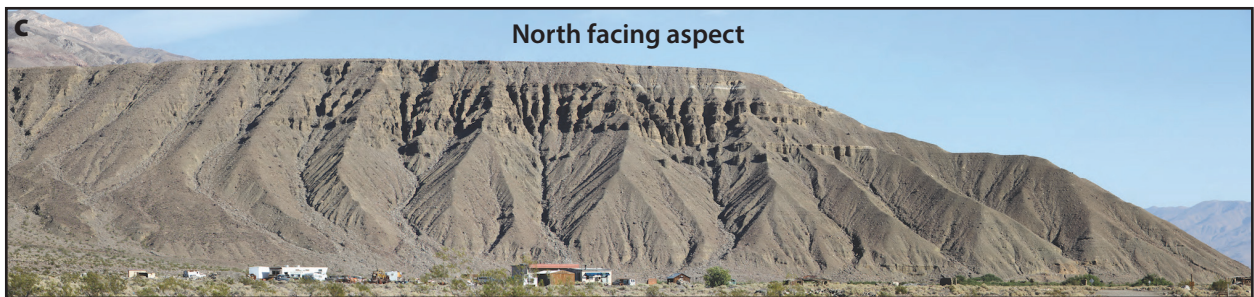
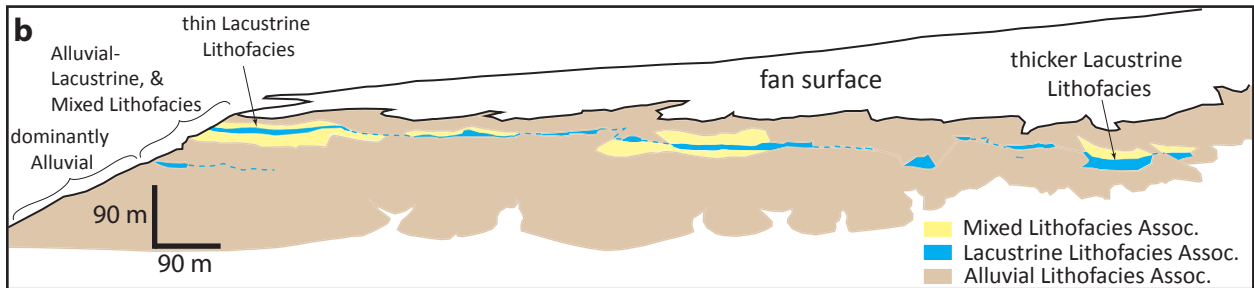


Figure 5

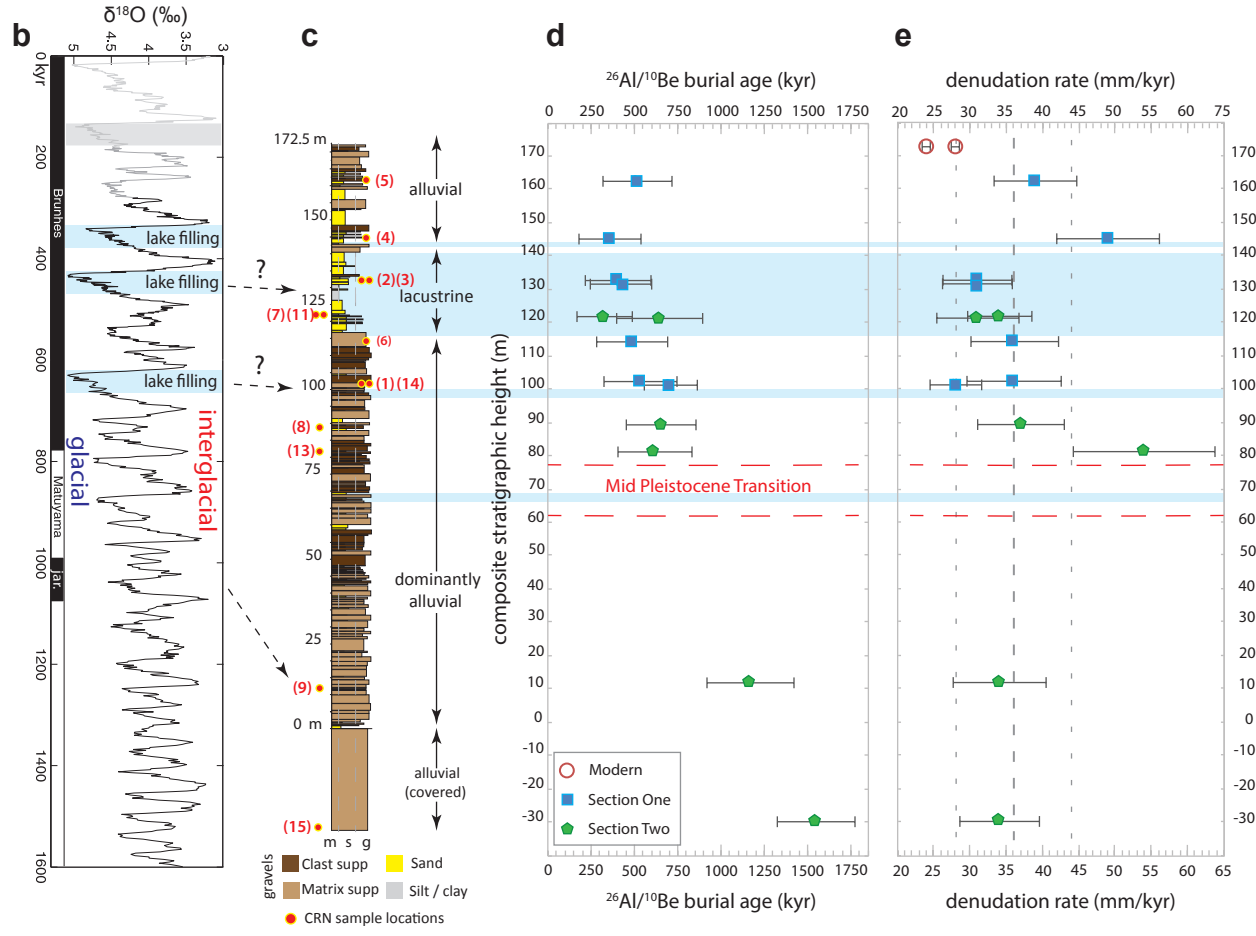
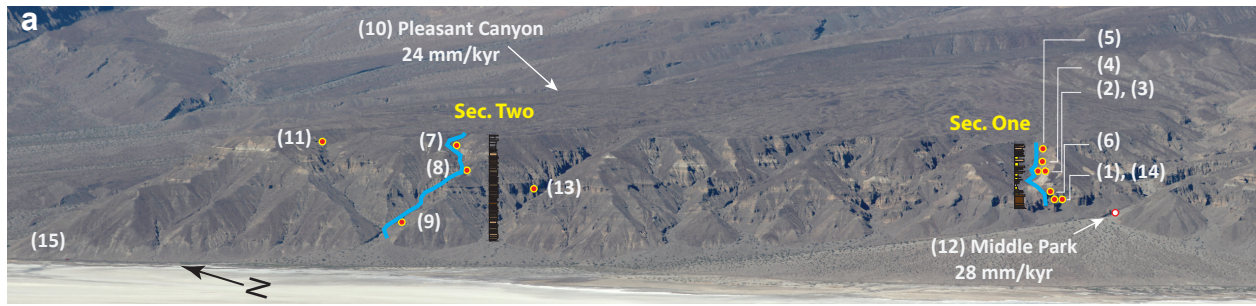


Figure 6

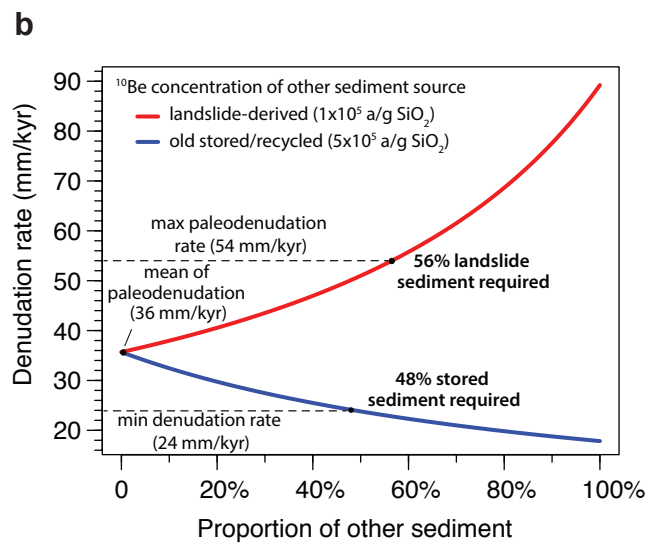
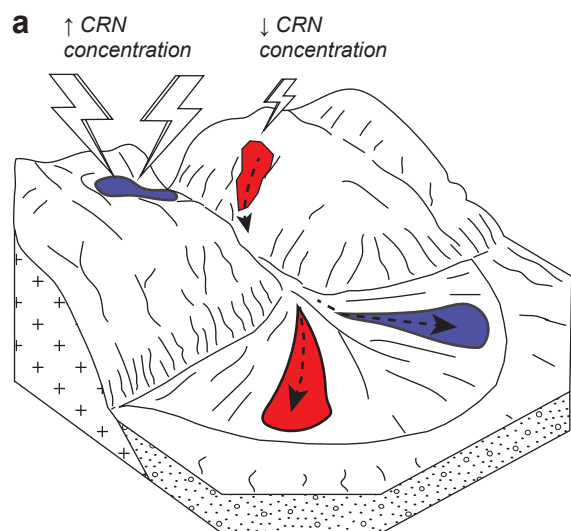
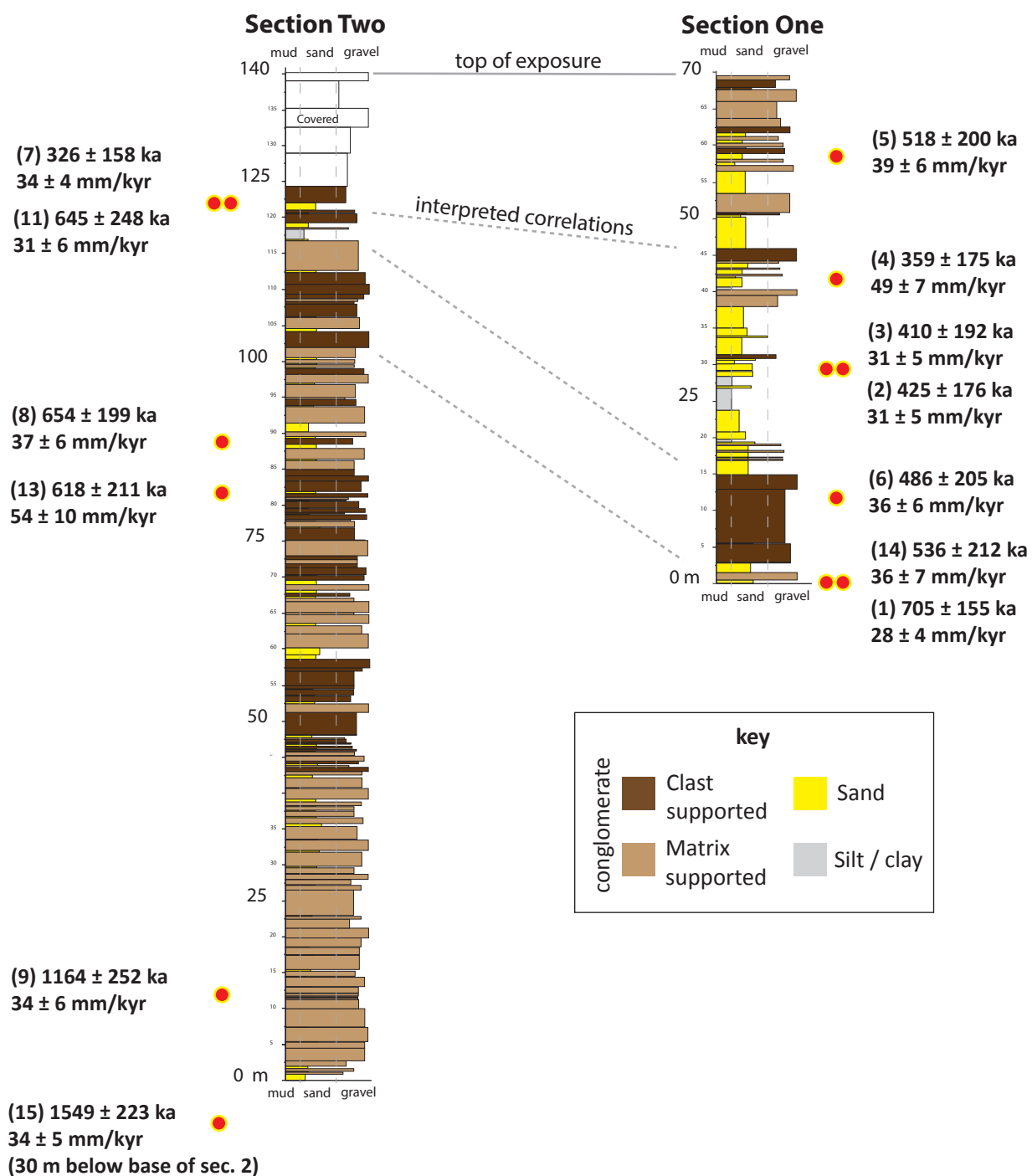


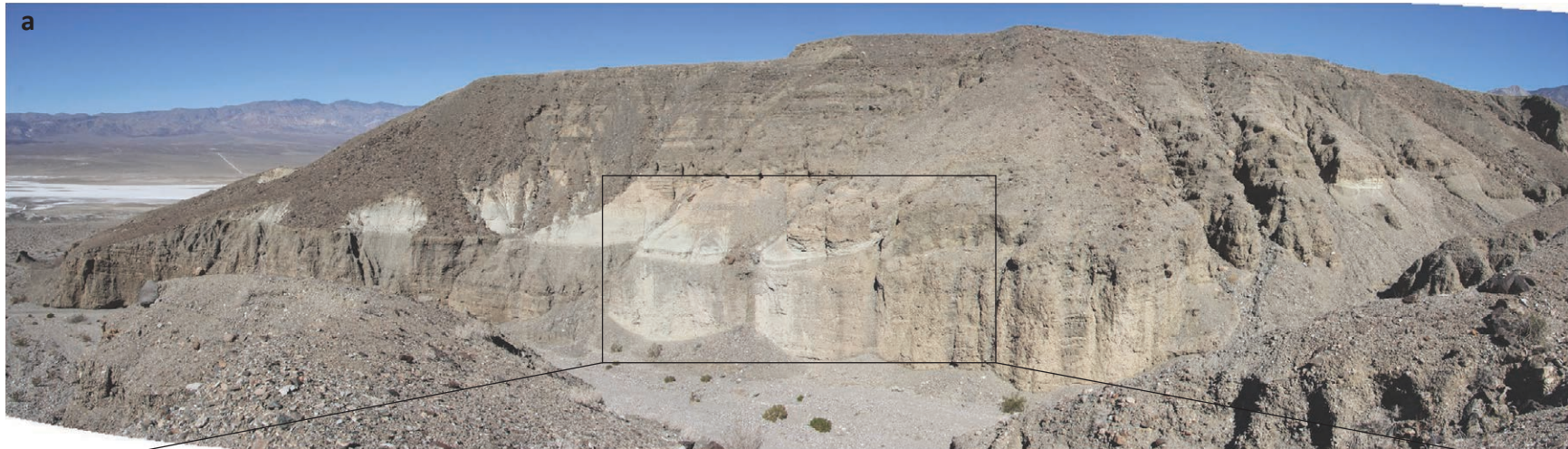
Figure 7



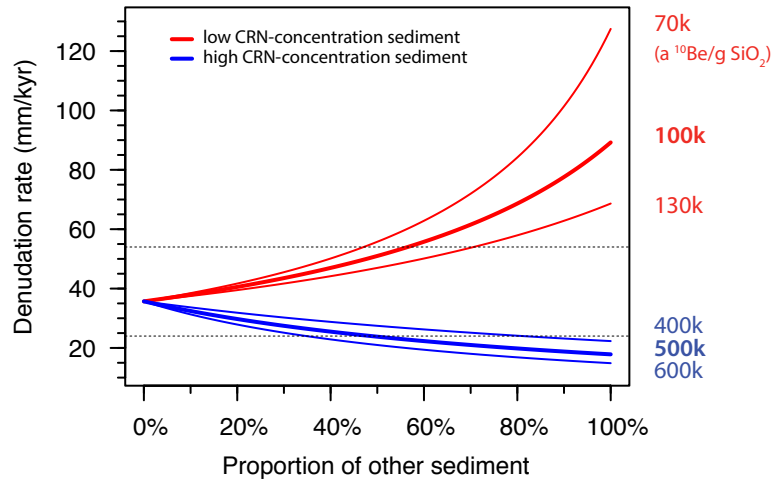
Suppl. Figure S1



Suppl. Figure S2.1



Suppl. Figure S2.2



Suppl. Figure S3